Atomic-level mechanisms of short-circuit diffusion in materials

Chesser, Ian Wallace
Koju, Raj K
MIshin, Yuri

To be published in: International Journal of Materials Research

DOI to publisher's version: 10.1515/ijmr-2023-0202

Review

Ian Chesser, Raj K. Koju and Yuri Mishin*

Atomic-level mechanisms of short-circuit diffusion in materials

https://doi.org/10.1515/ijmr-2023-0202
Received June 21, 2023; accepted September 20, 2023;
published online January 29, 2024

Abstract: This paper reviews the recent progress in understanding the atomic mechanisms of short-circuit diffusion along materials interfaces, such as grain and interphase boundaries, as well as lattice and interfacial dislocations/disconnections. Recent atomistic computer simulations have shown that short-circuit diffusion is dominated by collective atomic rearrangements in the form of strings and rings of mobile atoms. The process is dynamically heterogeneous in space and time and has many features in common with atomic dynamics in supercooled glass-forming liquids. We discuss examples of grain boundary, interphase boundary, and dislocation diffusion in metals and alloys, including the solute effect on the diffusion rates and mechanisms. Interphase boundaries are exemplified by Al–Si interfaces with diverse orientation relationships and atomic structures. The hierarchy of short-circuit diffusion paths in materials is reviewed by comparing the rates of grain boundary, interphase boundary, and dislocation diffusion. Future directions in the field of short-circuit diffusion in defect core regions are discussed.

Keywords: Atomistic modeling; Diffusion; Interphase boundary; Grain boundary; Dislocation

1 Introduction

It is well-established that the atomic mobility in core regions of extended crystalline defects in materials greatly exceeds the atomic mobility in the perfect crystalline lattice (*1–7*). The phenomenon is often referred to as short-circuit diffusion by analogy with electric current finding a low-resistance path in an otherwise high-resistance medium. Short-circuit diffusion along dislocation lines is alternatively called "pipe diffusion". The diffusivity difference between the defect cores and the perfect lattice can reach many orders of magnitude, causing significant impacts on physical and mechanical properties of materials.

This paper focuses on diffusion along grain boundaries (GBs), interphase boundaries (IPBs), and dislocations. Self-diffusion and solute diffusion along these defects control many processes in structural and functional materials, including microstructure evolution, phase transformations, creep deformation, sintering, and oxidation – to name a few (*8*). For example, the high-temperature creep performance of metal–matrix composites depends on shear resistance of the metal–ceramic interfaces (*9*), which is kinetically controlled by diffusive mass transport along these interfaces (*10*). As another example, atomic transport along dislocations is one of the mechanisms of creep deformation (*11–13*) and dynamic strain aging in alloys (*14–16*). Dislocation diffusion can also accelerate the coarsening of second-phase inclusions in precipitation-strengthened alloys (*17*).

In addition to the practical significance, short-circuit diffusion is a phenomenon of great fundamental interest. The defect core regions are generally less ordered than the crystalline lattice and can exhibit enormous structural complexity. They are embedded in a highly ordered lattice environment and represent a unique state of matter transitional between disordered (bulk liquid) and ordered (perfect crystal). The interface structure is squeezed between *differently* oriented crystals and is forced into a *frustrated quasi-2D state*.

While a large volume of experimental diffusion data has been accumulated over the past decades (*1–7*), the current understanding of diffusion mechanisms in defect core regions remains highly incomplete. The experimental diffusion measurements are based on the phenomenological Fick's law of diffusion specialized to the appropriate geometries and boundary conditions. The extracted diffusion coefficients represent a convolution of many

***Corresponding author: Yuri Mishin**, Department of Physics and Astronomy, George Mason University, 4400 University Drive, MSN 3F3, Fairfax, VA 22030-4444, USA, E-mail: ymishin@gmu.edu, http://physics.gmu.edu/~ymishin/
Ian Chesser, Department of Physics and Astronomy, George Mason University, MSN 3F3, Fairfax, VA 22030, USA; and Computational Physics Division, Los Alamos National Laboratory, Los Alamos, NM 87545, USA, E-mail: ichesser@lanl.gov
Raj K. Koju, Department of Physics and Astronomy, George Mason University, MSN 3F3, Fairfax, VA 22030, USA, E-mail: rkoju@masonlive.gmu.edu

atomic-level events averaged over the macro- or mesoscopic length and time scales of the diffusion experiments. Such measurements cannot provide reliable information about the *microscopic* diffusion mechanisms. Diffusion mechanisms in bulk crystalline solids have been studied by experimental methods providing some access to diffusive events on the atomic scale (*18*), such as quasi-elastic neutron scattering (*19, 20*) and perturbed angular correlations (*21*). Additional information can be extracted from the isotope effect measurements and the pressure dependence of diffusivity (*18*). However, applications of such methods to dislocation cores or interfaces are virtually non-existent, and would be extremely difficult given the complexity of the defect core structures and the relatively small fraction of atoms residing in the core regions. Some suggestions regarding possible diffusion mechanisms have been proposed by combining the measured diffusion coefficients with assumed microscopic models. However, such models are usually based on several layers of assumptions and crude approximations making the conclusions only suggestive at best. For example, in the recent study of Co and Ag GB diffusion in severely deformed α-Ti polycrystals (*22*), possible GB diffusion mechanisms were proposed by assuming that Co and Ag diffuse in the GBs interstitially and substitutionally, respectively, because they do so in the perfect lattice. It was further assumed that Co diffusion is subject to a trapping effect previously proposed for hydrogen diffusion in Pd. A set of further assumptions had to be made linking the traps to plastic deformation.

The lack of *direct* access to the microscopic information inherent in the existing experimental methods explains why nearly all existing knowledge of the interface and dislocation diffusion mechanisms comes from atomistic computer simulations.

The goal of this paper is to review the recent progress in understanding the interface and dislocation diffusion mechanisms by means of atomistic simulations. We start by reviewing the methodology for computing the diffusion coefficients in defect core regions and investigating the respective diffusion mechanisms (Section 2). Section 3 starts with a brief review of the well-established knowledge of GB diffusion. The rest of this Section is focused on the most recent research extending the prior work to alloy systems and uncovering detailed information about diffusion mechanisms. Section 4 addresses a more complex and less understood type of materials interface. Diffusion along metal–nonmetal IPBs is an open field in which reliable results are only beginning to emerge. This Section reviews the recent work on Al–Si IPBs, comparing the computed diffusivities with those for GBs and discussing the underlying mechanisms. The third case of short-circuit diffusion along dislocation lines is the subject of Section 5. We highlight recent atomistic simulations that predict the dislocation diffusion coefficients in Al–Si alloys, compare them against GB and IPB diffusivities in this system, and provide a glimpse into dislocation diffusion mechanisms. Finally, in Section 6 we summarize this review and outline outstanding problems for future research.

2 Methodology

2.1 A historical perspective

The methodology of short-circuit diffusion calculations underwent a significant evolution over the past two decades. Earlier work was focused on GBs in elemental solids and primarily utilized molecular statics (MS) in conjunction with kinetic Monte Carlo (KMC) simulations (*23–28*). The GB structure was assumed to be perfectly ordered except for a small concentration of vacancies and interstitials. Point-defect free energies at various GB sites were calculated by MS and the quasi-harmonic approximation and used to predict the equilibrium point-defect concentrations. Migration barriers were computed for a set of defect jumps, and the respective jump rates were calculated within the transition state theory. The jump rates were compiled in a rate catalog, which was fed into a KMC simulation of the defect's random walk along the GB. Combined with the defect concentrations, the KMC simulations yielded the self-diffusion coefficients. They also provided information about diffusion anisotropy and the relative contributions of vacancies and interstitials to the diffusion flux. Similar techniques were employed to study dislocation pipe diffusion (*14, 29–33*). The obvious drawback of this approach is the assumption that the GBs and dislocation cores maintain perfectly ordered, zero-Kelvin atomic structures at all temperatures. Clearly, this assumption is only appropriate at low homologous temperatures. Another assumption is that the short-circuit diffusion is mediated by random walk of single point defects, which is also only valid at low temperatures, and moreover, rules out a discovery of many alternative mechanisms.

The growing computer power and the development of more advanced simulation algorithms and software over the past 10–15 years have made it possible to extend the diffusion simulations to higher temperatures and more realistic defect structures. Another important factor was the development of more accurate and reliable interatomic potentials. The MS/KMC approach was replaced by *direct* molecular dynamics (MD) simulations. MD trajectories

provide access to all details of the atomic movements without any approximations other than those built into the interatomic potential. Some restrictions exist due to the length and time scale limitations of MD, but they are not as severe as for lattice diffusion thanks to the greatly enhanced atomic mobility in the defect cores. The MD simulations performed over the recent years have greatly expanded our understanding of defect core structures at high temperatures and have revealed new diffusion mechanisms drastically different from the mechanisms of lattice diffusion. In what follows, we will primarily focus on the modern MD-based methods of diffusion simulations.

2.2 Interatomic potentials

Large-scale MD simulations rely on classical interatomic potentials (*34–37*), which constitute the critical ingredient of the methodology. The accuracy of the potentials largely determines the reliability of the MD results and the conclusions drawn from the simulations. Interatomic potentials may come in many different forms, depending on the material simulated. For metals and metallic alloys, the embedded-atom method (EAM) (*38–40*), modified EAM (MEAM) (*41*), and angular-dependent potential (ADP) (*42*) are employed as they are specifically designed to capture the nature of metallic bonds. Another class of cluster expansion potentials has been proposed by Drautz (*43–45*). For strongly covalent materials, such as silicon and carbon, the Tersoff (*46–48*) and Stillinger–Weber (*49*) potentials are more appropriate. The metallic and covalent potentials have significantly different functional forms reflecting the differences in the underlying physical and chemical models. This incompatibility of the functional forms makes it extremely difficult to model mixed-bonding systems such as metal–ceramic interfaces. One proposed option (*50–52*) is to represent metal–nonmetal interactions by generalized functions that mathematically reduce to the respective single-element functions under certain combinations of parameters. Because such generalized functional forms are not rooted in mixed-bonding physics, achieving high accuracy with such potentials remains a challenge.

During the past decade, a new class of machine-learning (ML) potentials has emerged, which is based on a different philosophy than the traditional potentials (*37*). The physics of interatomic bonding is no longer considered beyond the principles of locality of atomic interactions and translational/rotational invariance of energy. The local environment of every atom (expressed through a set of geometric descriptors) is mapped directly onto the potential energy surface using a high-dimensional nonlinear regression, such as the Gaussian process regression (*53–59*), the kernel ridge regression (*60–62*), an artificial neural network (NN) (*37, 63–77*), the spectral neighbor analysis (*78–80*), or a moment tensor potential (*81*). The regression model depends on a large ($\sim 10^3$) number of parameters, which are trained on a database composed of 10^3 to 10^4 supercells whose energies and forces are obtained by high-throughput first-principles calculations. A high accuracy of fitting can be achieved, usually on the level of meV/atom. Despite the high promise of ML potentials, their application to diffusion simulations is at early stages. ML potentials are computationally slower than the traditional potentials, which presents a challenge to large-scale MD simulations. Transferability to unknown atomic configurations is another concern (*37*). Nevertheless, ML potentials have a significant potential for diffusion applications in the future.

2.3 System preparation

GBs are created by standard crystallographic constructions in a rectangular simulation block with periodic boundary conditions in the (x, y) plane parallel to the GB. The GB structure is optimized to achieve the lowest possible energy by a grid search, in which hundreds of rigid displacements parallel to the GB plane are applied to one of the grains followed by removal of closely spaced atoms and static relaxation (*25, 82, 83*). More sophisticated optimization protocols can also be applied that adjust the atomic density in the GB core. The latter step often reveals new GB structures not found by the grid search (*84–86*). In alloys, the GB must be additionally equilibrated with respect to the distribution of the chemical components across the system. This is usually accomplished by canonical or semi-grand canonical Monte Carlo (MC) simulations, in which the chemical identities of the atoms are swapped in pairs or switched to an alternative chemical species. The chemical equilibration often creates GB segregation, which can impact GB diffusion (*87–89*).

For IPBs, the interface construction is more complex (*90*). The phases need to be elastically strained to accommodate the lattice misfit. To minimize the strain effect on diffusion, the interface area must be large enough to reduce the misfit strain. For IPBs between binary or multicomponent phases, chemical equilibration by MC is required to ensure thermodynamic equilibrium between the bulk phases and equilibrium distribution of the alloy components in the interface region. This, in turn, requires the knowledge of the relevant part of the bulk phase diagram computed with the interatomic potential. Furthermore, sufficiently stable crystallographic relationships between the phases must be found that represent the real alloys and do not change during the diffusion simulations.

For dislocation diffusion, a single straight dislocation is created in a cylindrical simulation block with periodic boundaries along the cylinder axis x to mimic an infinitely long dislocation line. An important step is to create a strain field around the dislocation representing the field in an infinitely large system as closely as possible. This can be achieved by displacing the atoms according to the elastic strain field predicted by the anisotropic linear elasticity solution (*91, 92*) with elastic constants computed with the interatomic potential. In alloys, the open-system elastic constants must be used (*93, 94*). Atoms in a thin outer shell of the cylinder are fixed in their displaced positions while the remaining atoms are dynamic. As for interfaces, MC simulations are performed to create a solute segregation atmosphere around the dislocation line.

In all three cases (GBs, IPBs, dislocations), thermal stresses that can arise during the simulations are removed by using a thermally expanded lattice parameter corresponding to the simulation temperature. Most diffusion studies employ the Large-scale Atomic/Molecular Massively Parallel Simulator (LAMMPS) package (*95*) for MD and MC simulations. For more advanced MC simulations, the Para-GrandMC (PGMC) code (*96–98*) can be used that implements massively parallel MD and MC in a variety of statistical ensembles. The software package OVITO (*99*) is typically utilized to visualize and analyze the defect core structures.

2.4 Diffusion simulations

2.4.1 Calculation of diffusion coefficients

The calculation of diffusion coefficients starts with a canonical MD simulation to bring the system to thermal equilibrium at the chosen temperature. The MD ensemble is then switched to microcanonical (NVE), and a long (up to tens of nanoseconds) production run is performed. The NVE ensemble is preferred over the canonical ensemble because it eliminates any possible impact of the thermostat on spontaneous diffusive events. For GBs and IPBs, atomic trajectories in a 1–2 nm thin layer centered on the interface are tracked during the simulation. The trajectories are used to compute the diffusion coefficients in the in-plane x and y directions from the Einstein relations $D_x = \langle x^2 \rangle / 2t$ and $D_y = \langle y^2 \rangle / 2t$, where $\langle x^2 \rangle$ and $\langle y^2 \rangle$ are the respective mean squared displacements (MSDs) of the atoms. Linearity of the MSD versus time is checked, and the diffusion coefficient is averaged over multiple simulation runs with different velocity seeds. The ratio D_x/D_y obtained is a measure of the interface diffusion anisotropy. For alloys, the diffusivities of individual chemical species are computed. To collect adequate statistics of MSDs, the simulations are conducted at relatively high temperatures, typically above $0.6–0.7T_m$ (T_m being the melting point).

The dislocation case is more complex because the diffusivity D falls off with the distance R from the core slower than for interfaces. One proposed solution is to approximate $D(R)$ by a Gaussian peak of height D_{max} and width δ centered at the core. The average diffusivity $\overline{D}(R)$ is calculated by applying the Einstein equation $D = \langle x^2 \rangle / 2t$ to atomic trajectories within cylindrical regions with different radii R centered at the dislocation line. The function $\overline{D}(R)$ obtained is fitted by the equation

$$\overline{D}(R) = D_{max} \frac{\delta^2}{R^2} \left(1 - e^{-R^2/\delta^2}\right) + D_L \quad (1)$$

with three parameters D_{max}, δ, and D_L. The latter has the meaning of the lattice diffusivity and, in most cases, can be neglected compared to the first term. The effective dislocation core diffusivity can be evaluated by $D = D_{max}/e$.

2.4.2 Investigation of diffusion mechanisms

As will be discussed later, the defect core diffusion at high temperatures is dominated by collective diffusion mechanisms. Such mechanisms are investigated by statistical tools developed to study atomic dynamics in supercooled liquids and glasses (*100–107*). It should be emphasized that at typical simulation temperatures, interfaces and dislocations can freely exchange point defects with the surrounding lattice. Point defects jumping out of interfaces and dislocations have been observed in several systems (*33, 88, 89, 108, 109*). Thus, the defect cores are not closed systems and are not subject to a conservation constraint. In addition to Frenkel pairs, single defects can also freely form in defect core regions and cause short-circuit diffusion.

The collective nature of the diffusive events manifests itself in the clustering of simultaneously moving (dynamic) atoms in the defect core (*90, 102, 105, 109, 110*). The dynamic atoms are identified as atoms with the net displacement Δr during a preset time interval Δt lying within the range $0.4r_0 < \Delta r < 1.2r_0$, where r_0 is the first nearest-neighbor distance in the lattice. Here, the upper bound eliminates atoms that had undergone multiple hops and the lower bound eliminates immobile atoms. Next, pairs of mobile atoms (i, j) are found that remain neighbors after the time Δt. For such atoms, $|\mathbf{r}_i(0) - \mathbf{r}_j(0)| < r_0$ and $|\mathbf{r}_i(\Delta t) - \mathbf{r}_j(\Delta t)| < r_0$ (*110*). To identify atomic groups moving as a chain, pairs of mobile atoms are found such that one atom jumps into the previous position of the other during the time Δt. Such pairs are found from the criterion $\min(|\mathbf{r}_i(\Delta t) - \mathbf{r}_j(0)|, |\mathbf{r}_j(\Delta t) - \mathbf{r}_i(0)|) < 0.43r_0$ (*109*). (The specific number

0.4, 1.2 and 0.43 are hyper-parameters that may depend on the particular system.) Mobile pairs containing common neighbors are considered to belong to the same mobile cluster. Standard cluster analysis is performed to reveal all mobile clusters and analyze their size distribution and geometric properties. For example, the cluster's gyration radius R_g can be fitted by the function $R_g \propto n^d$, where n is the number of atoms in the cluster, to find the cluster's fractal dimension d. Clusters of immobile atoms can also be identified. They form their own distribution that also contains information about the diffusion mechanisms.

Other statistical measures of collective atomic motion can also be calculated, such as the atomic displacement distribution function, the direct-space van Hove correlation function, and the jump-direction correlation function (*110*). In alloy systems, the diffusion mechanisms of each species can be investigated as a function of temperature and chemical compositions.

3 Grain boundary diffusion

As mentioned above, low-temperature GB diffusion mechanisms were studied by MS/KMC simulations assuming a perfectly ordered GB structure. In this approach, a single vacancy or a single interstitial is introduced into the GB core by removing or adding a single atom. The defect migrates along the GB, causing diffusive jumps of GB atoms. The point defect properties and the atomic movements are analyzed to determine the diffusion mechanisms (*24–26, 28, 90, 109–112*). The results of such studies can be summarized as follows.

The point defect formation energy in GBs is on average lower than in the lattice with large site-to-site variations. The average vacancy and interstitial formation energies are close to each other, in contrast to the lattice, where interstitials have a significantly higher formation energy than vacancies. Relaxed point defect structures in GBs are often delocalized over an extended region comprising 5 to 7 atoms. Some GB sites do not support a stable vacancy: when an atom is removed, the vacant site is immediately filled by a neighboring atom. As a result, the vacancy is formed at the neighboring site, not where it was intended. GB atoms can move by individual jumps or collective displacements involving several atoms moving simultaneously. The moving atoms often form a string, in which the head atom fills a relatively open space while the trailing atom leaves a similar open space behind. Occasionally, the string can be closed to itself, forming a ring of atomic displacements.

At high temperatures, the GB structure becomes increasingly disordered. Some GBs premelt transforming into a liquid-like layer squeezed between two crystals (Figure 1). The concept of individually moving point defects no longer applies. The GB diffusivity must be determined by direct MD simulations. Typical simulation results are presented in Figure 2 for GB diffusion in Cu and Al. These and other results reported in the literature lead to the following conclusions:

– Diffusion in tilt GBs is significantly anisotropic, especially at relatively low homologous temperatures. Diffusion along the tilt axis is usually faster than in the perpendicular direction.
– GB diffusivity strongly depends on GB crystallography. At moderate homologous temperatures, the diffusivities in different high-angle GBs in the same material spread over one to two orders of magnitude (*28, 109*).

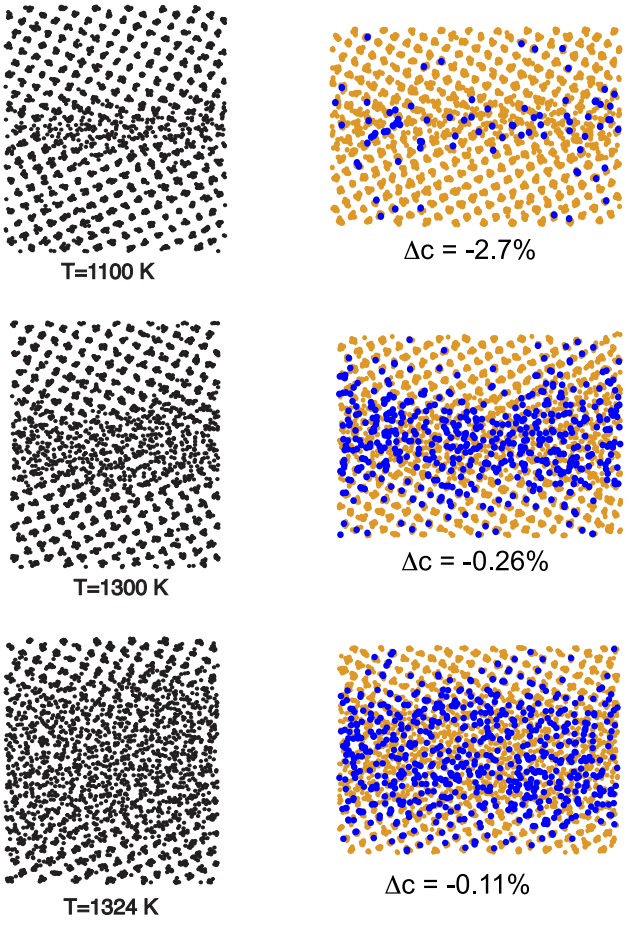

Figure 1: Premelting of the Σ5 (210) GB in Cu (*113*). The atomic positions are projected along the [001] tilt axis normal to the page. Left column: pure Cu GB at temperatures indicated under the images. The melting temperature of Cu with the interatomic potential used in the simulations is 1327 K. Right column: same GB in Cu–Ag solution at the temperature of 1100 K for different compositional deviations Δc (at.% Ag) from the solidus line.

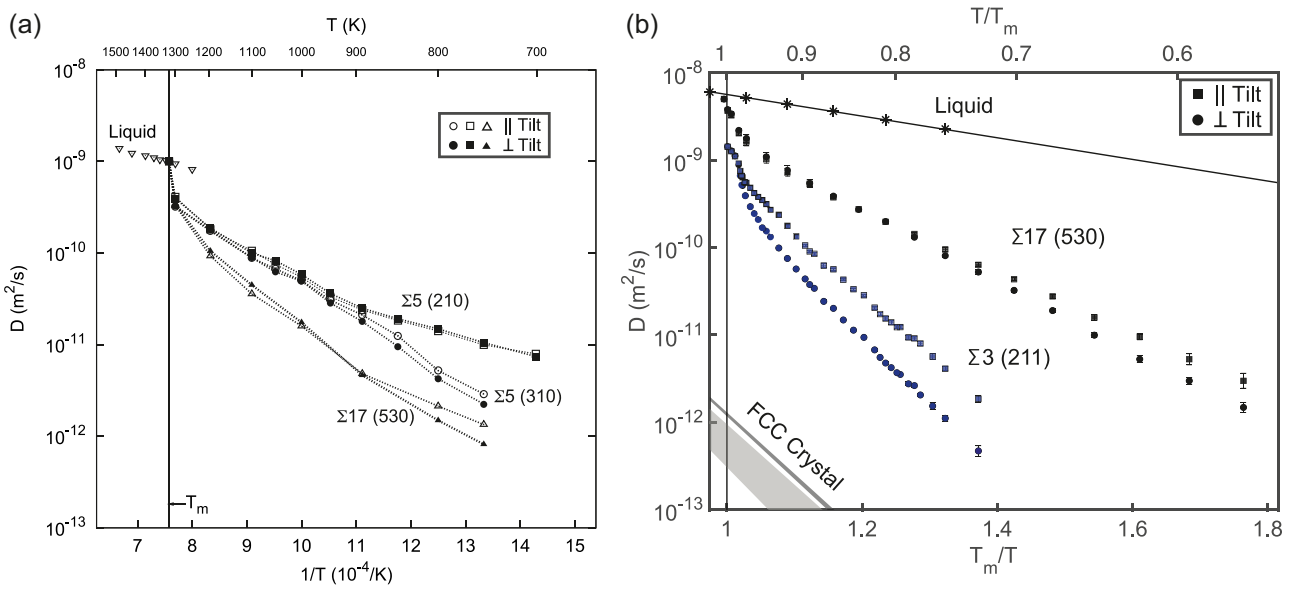

Figure 2: Typical Arrhenius plots of GB diffusion in (a) Cu (*28*), and (b) Al (*109*) obtained by MD simulations. The vertical line indicates the Al melting temperature T_m. The GBs are symmetrical tilt type and are labeled by the reciprocal coincident site density Σ and the GB plane.

The spread widens with decreasing temperature. Diffusion in low-angle GBs is several orders of magnitude slower than in high-angle GBs (*88*).

– At temperatures approaching the melting point, the GB diffusivity accelerates due to the premelting effect (Figure 2). In some high-angle GBs, it approaches the diffusivity in the bulk liquid phase, confirming that the GB structure becomes similar to a supercooled liquid. In the premelting regime, the diffusion coefficients in crystallographically different GBs merge together. GB diffusion becomes insensitive to GB structure. Low-angle and even some high-angle GBs do not premelt and can be overheated above T_m.

In elemental materials, the GB diffusivity generally correlates with GB energy (*28, 109*).

Simulation of GB diffusion in alloys is a relatively new direction and reliable results are only beginning to emerge. Segregation–diffusion relationships have been studied in Cu–Ag alloys by combined MC and MD simulations in the temperature–composition domain of Cu-based solid solutions (*87*). The GB diffusivities of Cu and Ag exhibit different composition and temperature dependencies. Depending on the temperature, they can correlate with each other, anti-correlate, cross, or have local minima as functions of chemical composition. These complex behaviors have been explained by an interplay between different diffusion mechanisms and competing physical effects, such as site blocking, site competition, and the onset of GB disordering due to premelting when the alloy composition and/or temperature approach the solidus line on the phase diagram. GB premelting (Figure 1) plays a greater role in alloys than in elemental materials. It typically starts at relatively low temperatures at which the same GB in the respective elements remains ordered (*28, 113–115*). GB premelting in alloys is fueled by GB segregation and can drastically alter the diffusion mechanisms.

In the Al–Mg system, Mg segregation slows down the Al GB diffusion compared with pure Al, an effect that was observed in both high-angle and low-angle GBs (*88*). High-angle GB premelting accelerates GB diffusion of both Al and Mg, and both diffusion coefficients approach the diffusivities in the liquid phase. More recently, Al and Si GB diffusivities were calculated in Al-based Al–Si alloys (*90*). Si was found to segregate to Al GBs and accelerate the GB diffusivity of Al relative to pure Al GBs with the same crystallography. Si was also found to diffuse in the segregated GBs slightly faster than Al. Note that this diffusion-segregation trend is opposite to that in the Al–Mg system (*88*), highlighting the fact that the interplay between GB diffusion and GB segregation is complex and system-dependent.

Diffusion mechanisms in partially or fully disordered GBs were studied by the statistical tools discussed in Section 2.4.2. Such studies provide strong evidence that GB atoms diffuse by collective rearrangements involving several to dozens of atoms at a time. The diffusive events (collective jumps) often occur in the form of strings or rings (strings closed to themselves) (Figure 3). These mechanisms are remarkably similar to those in disordered bulk systems

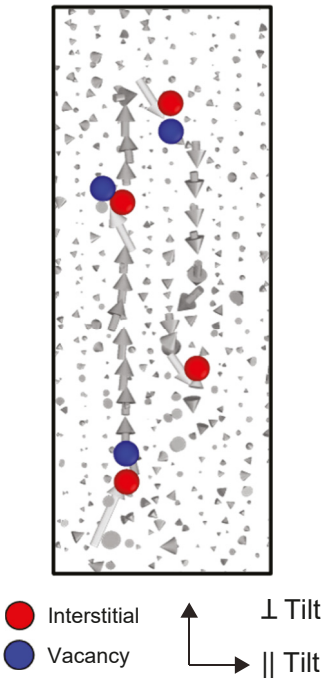

Figure 3: Examples of collective diffusion events in the Al Σ3 GB at the temperature of 700 K (0.75 T_m) involving the formation and multiplication of point defects (*109*). The arrows represent string-like atomic displacements during a 80 ps time interval. The displacements form a string with an interstitial and a vacancy at the head and tail of the string, respectively. Note the two strings linked to each other and having a parallel alignment. The left-hand string facilitates the formation of the right-hand string.

such as supercooled liquids, glasses, and crystalline superionic materials (*101–107, 109, 116, 117*). Although these mechanisms are different from those in ordered GBs, some similarities still exist. As mentioned above, string-like atomic rearrangements were also found in well-ordered GBs, although the number of atoms involved is less than in disordered structures. Furthermore, while point defects cannot always be identified, disordered GB structures exhibit significant atomic density variations. Some atomic configurations resemble vacancies (low local density) while others resemble interstitials (high local density). Both can be identified automatically by suitable structure analyses.

A prominent feature of atomic dynamics in GBs, which is in common with disordered bulk systems, is the dynamic heterogeneity. Atoms undergoing diffusive rearrangements cluster together on length and time scales that depend on the underlying GB structure, temperature, and (in alloy systems) chemical composition. The clusters of mobile atoms have a fractal dimension close to $d = 1.5$ (*109, 110*). This value lies between 1D and 2D, reflecting the shape anisotropy (elongation) of the mobile clusters in the quasi-2D GB structure. Immobile atoms, likewise, form clusters with their own size distribution and time scale. The time evolution of mobile and immobile clusters can be conveniently visualized using space-time diagrams (*109, 118, 119*). Such diagrams are obtained by computing the atomic displacement fields during a suitable time interval and stacking them together along the time axis. An example of a space–time diagram is presented in Figure 4a for the Σ3 (incoherent twin) GB in Al (*109*). The diagram shows the formation and disappearance of mobile and immobile clusters in space and time. The immobile clusters appear as empty regions (bubbles (*109, 118, 120*)) separating the mobile clusters, which are strongly elongated along the time axis.

The nucleation of a mobile cluster is triggered by the formation of a Frenkel pair that grows into a string. The string triggers the formation of similar string-like excitations and new point defects in nearby GB regions, which in turn cause the formation of many additional strings and point defects. In other words, the initial local excitation spreads like an avalanche, creating a growing cluster with a large population of point defects and drastically enhanced atomic mobility. This mechanism of avalanche formation is known as dynamic facilitation (*109, 118, 119*), a process in which a local excitation spreads in a self-catalytic manner by increasing the probability of similar excitations in surrounding regions.

The dynamic facilitation manifests itself in the branching and coalescence of the diffusion trajectories on the space–time diagram (Figure 4a). As the defect population grows during the avalanche period, so does the probability of the mutual recombination of the defects. The growth continues until a bifurcation point is reached at which the process switches from defect multiplication to self-recombination. The growth of the mobile cluster stops and it begins to shrink. This kinetic transition defines the avalanche lifetime and the mobile cluster size (*109*).

As shown in Figure 4b, mobile clusters have a shorter average lifetime than immobile clusters. This time-scale separation is a hallmark of facilitated atomic dynamics (*109, 118, 119*). The spatial dimensions of the mobile clusters are measures of the avalanche size. The avalanche size distribution is exemplified in Figure 4c for the Al Σ3 GB. The plot shows that the avalanche regions are elongated parallel to the tilt axis and have a significant probability of reaching 10–15 nm and containing hundreds of atoms.

A surprising finding of the recent simulations of Al GBs (*109*) is the intermittent GB diffusion at moderate homologous temperatures. The effect is illustrated in Figure 5a showing a staircase behavior of the MSD of GB atoms as

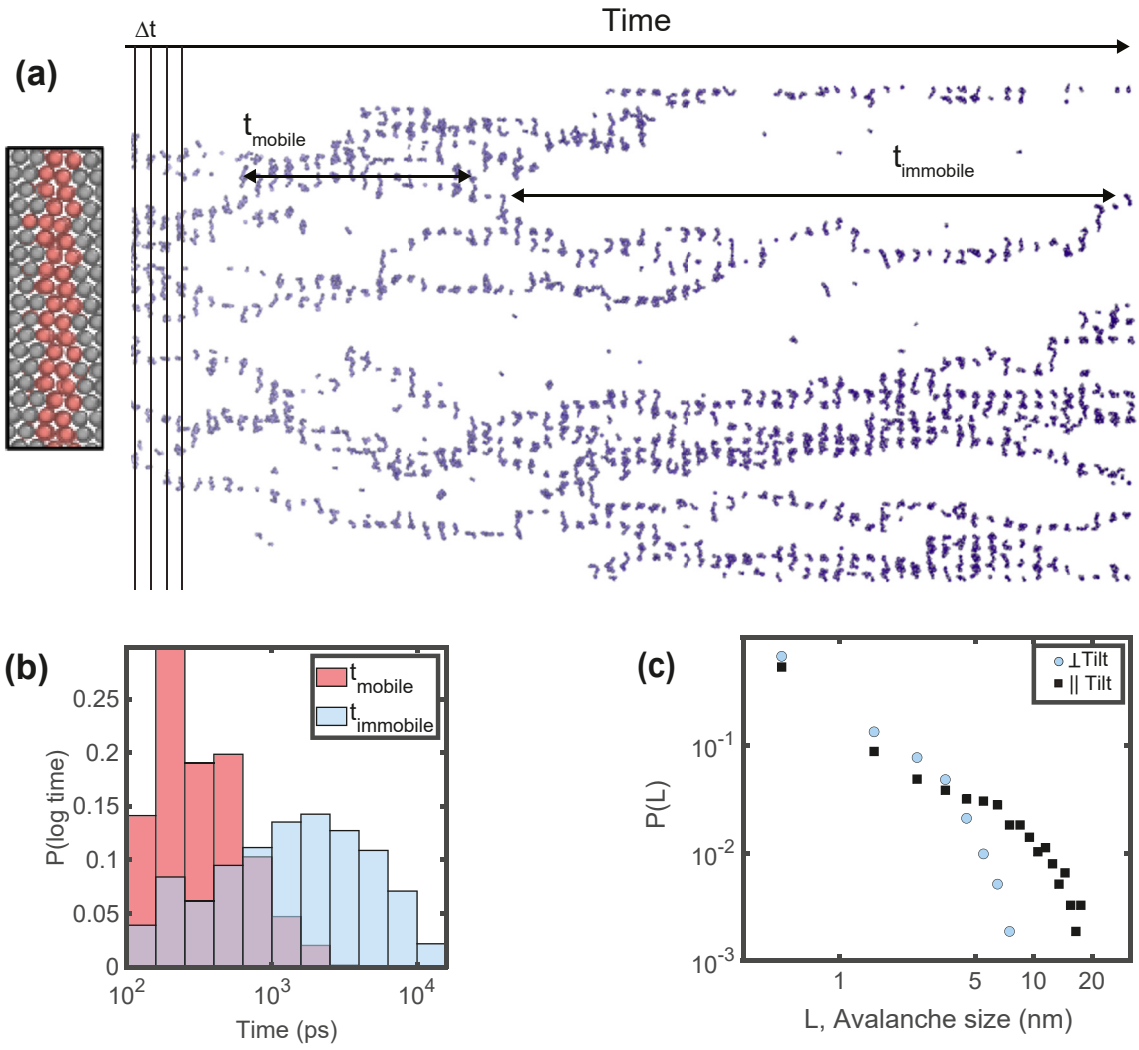

Figure 4: (a) Space–time atomic mobility diagram for the Al Σ3 GB computed with the time interval of 40 ps and viewed perpendicular to the tilt axis (*109*). The mobile/dynamic atoms are shown in dark blue. The immobile clusters are evident as elongated voids (bubbles) separating the mobile clusters. The arrows show examples of mobile and immobile cluster dimensions in time. (b) Probability distribution of lifetimes of mobile and immobile clusters. Note that immobile clusters persist on a longer time scale than mobile clusters. (c) Avalanche size distribution measured by the maximum dynamic cluster sizes perpendicular and parallel to the tilt axis. The separation of the two sizes shows that the dynamic clusters are elongated parallel the tilt axis. Note that the cutoff size along the tilt axis is larger than 10 nm.

a function of time. The slope of the plot is not constant as predicted by Einstein's equation but instead fluctuates around an average line. The atomic mobility randomly switches from very high (large slope) to very low (nearly horizontal slope). Analysis shows (*109*) that the surges of the GB diffusivity are caused by point-defect avalanches that spontaneously nucleate and spread across the GB area, while the low-diffusivity periods occur when the GB area is dominated by an immobile cluster. This explanation of the diffusion intermittency was confirmed by direct observations of atomic displacement fields. As an example, Figure 5c and d shows that the bursts of the point-defect population correlate with the large-slope portions of the MSD curves.

Based on this understanding of the diffusion intermittency, one can predict that it must disappear when the GB area is sufficiently large. Indeed, in a large GB area, multiple avalanches can randomly form at different locations. The diffusion coefficient represents the atomic mobility averaged over multiple avalanches and must exhibit a smooth and size-independent behavior. At the chosen simulation temperature, the avalanche size can reach 15–20 nm as shown in Figure 4c. Thus, the diffusion intermittency must exist in GBs with areas smaller than 15–20 nm and

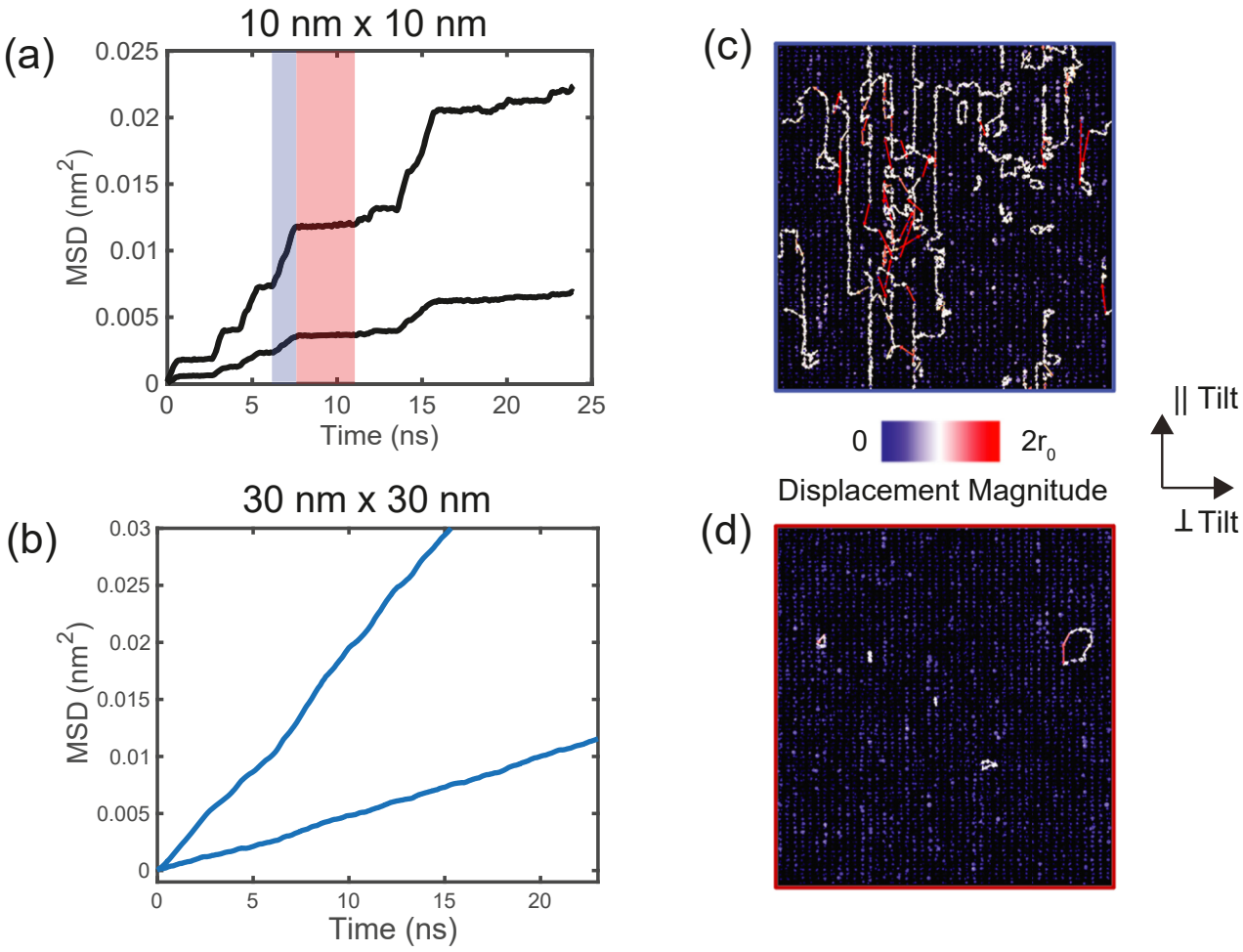

Figure 5: Example of intermittent diffusion behavior in the Al Σ3 GB: (a) atomic MSD as a function of time at 710 K (0.77 T_m) for the GB cross-sections of (a) 10 nm × 10 nm and (b) 30 nm × 30 nm. (c and d) Typical atomic displacement diagrams during the (c) avalanche and (d) locked time periods corresponding to the blue and red regions in (a). The GB plane is parallel to the page. The arrows represent atomic displacements during 1.2 ns and 3 ns time intervals and are colored by the displacement magnitude. The scale bar has units of the first nearest neighbor distance r_0.

vanish in GBs with larger areas. This is indeed observed in Figure 5 showing the significant diffusion intermittency in the 10 nm × 10 nm GB and smooth MSD curves in the 30 nm × 30 nm GB (Figure 5b).

The intermittent diffusion behavior in small GB areas is a general phenomenon observed in several crystallographically different GBs in different materials modeled with different interatomic potentials (*109*). An important lesson for future diffusion simulations is that the GB size matters. If the GB size is smaller than the avalanche size, the atomic MSDs can strongly fluctuate in time, leading to inaccurate GB diffusion coefficients. For accurate calculations, convergence tests must be performed to find a GB area large enough to exceed the avalanche dimensions. In experiments, nanoscale GBs can exhibit intermittent atomic dynamics creating additional noise in functional properties in the GHz frequency range.

Although the discussion above was focused on fcc metals, diffusion mechanisms in bcc metals have also been investigated, see for example (*112, 121, 122*).

GB diffusion mechanisms were also examined in Al–Si alloys, focusing on the incoherent twin boundary as an example (*90*). The mechanisms remain generally similar to those in pure Al, but the alloy composition offers a new degree of freedom for controlling the dynamic length and time scales. It was found that the segregated Si atoms participated in the collective events, as demonstrated in Figure 6. They refined the length scale of the collective atomic motion compared with pure Al. For example, the average string length was computed at 700 K for the time interval that

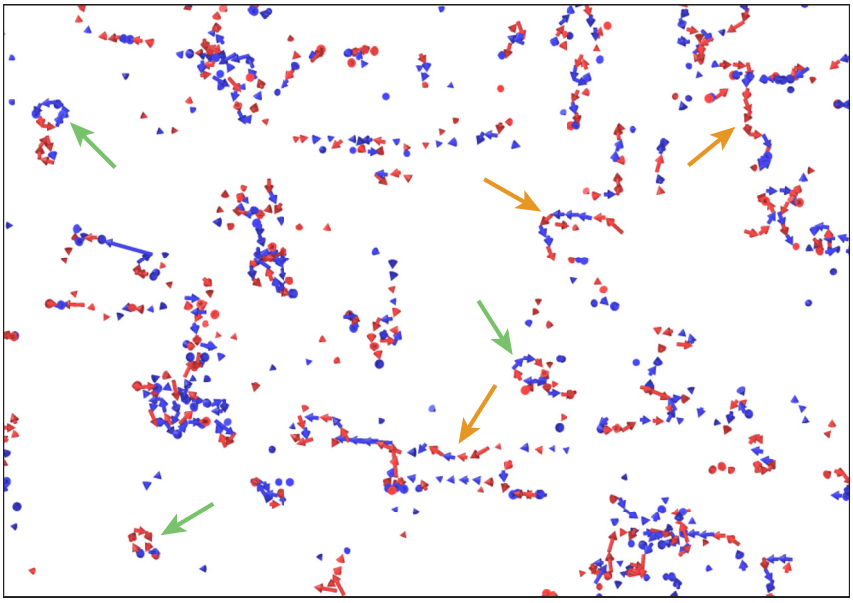

Figure 6: Illustration of collective diffusive events in the Σ3 GB in the Al–8 at.% Si alloy at the temperature of 700 K. The GB plane is parallel to the page. The red and blue arrows represent displacements of Al and Si atoms, respectively, in the GB core. The orange and green arrows point to examples of strings and rings, respectively.

maximized the string length. In pure Al, the average string contained around 5.5 atoms, whereas in the alloy, around 3 atoms. These observations have a preliminary character and await confirmation and expansion by more detailed investigations in the future.

4 Interphase boundary diffusion

4.1 Motivation

IPB diffusion has not been studied as well as GB diffusion either experimentally or by simulations. Many gaps of knowledge exist, especially regarding the diffusion mechanisms. Diffusion along metal–metal IPBs was measured in several systems in the 1990s (*1, 2, 123, 124*) but little work has been done after that. Much less is known about diffusion along metal–nonmetal interfaces. The only direct experimental measurement known to us was for indium chemical diffusion along Sn–Ge twist interfaces (*125*). Among less direct measurements, diffusion of Au and Ni along Ni/sapphire interfaces was back-calculated from the kinetics of partial solid-state dewetting of a Ni film from a sapphire substrate (*126–128*).

Recent years have seen an increased interest in atomic dynamics at Al–Si interfaces. The primary motivation for choosing this system is related to the problem of high-temperature creep in metal-matrix composites. At high temperatures, the metal–ceramic interfaces lose their shear resistance and the creep strength of the composite drastically deteriorates (*129*). The microscopic mechanisms governing the interfacial sliding at high temperatures remain largely unknown, but it is safe to assume that the process is controlled by diffusive mass transport along the metal–ceramic interfaces. The Al–Si system can serve as a prototype of a composite structure as it combines a soft metal with a hard covalent material representing the ceramic phase. The system features a simple eutectic phase diagram with low mutual solubility in the solid state, making it ideal for a fundamental study.

Diffusion along Al–Si interfaces has been recently studied by combined MD and MC simulations integrated with other modeling and structural analysis methods (*90*). A semi-empirical interatomic potential (*52*) was chosen to represent the atomic bonding in the Al–Si system. This binary potential is based on the Stillinger–Weber potential for Si (*49*) and the EAM-type Al potential developed by Mendelev et al. (*130*). Both potentials have been tested for many physical properties and widely used in numerous simulation studies. The cross-interaction functions were adjusted to reproduce DFT data for intermetallic compounds and the heats of formation of solid and liquid solutions in the Al–Si system (*52, 131*). The Al–Si phase diagram predicted by this potential was calculated by the phase coexistence method (*132–135*) and found to be in semi-quantitative agreement with the experimental diagram (*90*).

4.2 Construction of interphase boundaries

A significant part of the work (*90*) was constructing the Al–Si IPBs with different orientation relationships and evaluating their structural stability during high-temperature anneals required for a diffusion study. This step of the simulation procedure must be discussed in more detail as it strongly impacts the diffusion calculations. The importance of the system preparation is not specific to Al–Si interfaces; any simulation study of IPB diffusion includes the interface construction as the critical step. In Reference (*90*), two methods were applied to create equilibrium IPBs: the phase bonding method and the simulated epitaxy.

In the phase bonding method, the interface was constructed by bonding together Al and Si grains with chosen crystallographic orientations. The initial interface was subjected to a hybrid MC/MD anneal to establish phase equilibrium. During the anneal, the Al grain was allowed to slide past the Si substrate to accommodate possible sliding events that could lead to a deeper relaxation. Note that the initial orientation relationship between the phases could not change during the anneal.

In the simulated epitaxy method, the Si substrate with a chosen crystallographic orientation was brought in contact with a liquid Al layer. This was achieved by a multi-step process starting from an equilibrated bonded interface, separating the phases, equilibrating the Si surface, melting the Al phase by raising its temperature above T_m, re-establishing the contact between the phases, and finally quenching the liquid Al layer to a chosen temperature below T_m. During the subsequent MD simulation, the liquid Al layer solidified in a preferred crystallographic orientation relative to the Si substrate. This method is ideal for discovering new orientation relationships that are difficult to predict *a priori*. A downside of the method is that the solidification rate can be too high to ensure full thermodynamic equilibrium.

A broad exploration of different orientation relationships by the two methods (*90*) revealed a set of Al–Si interfaces that remained stable during the subsequent high-temperature anneals and a set of unstable interfaces. The stable orientation relationships were either cube-on-cube or twin-related type with small lattice rotations away from the ideal cubic or twinned orientation in some cases. Such interfaces did not premelt and could be overheated above the eutectic temperature. Some of the stable interfaces, such as $\{111\}_{Al}\|\{111\}_{Si}$ and $\{110\}_{Al}\|\{001\}_{Si}$, were previously observed in epitaxy experiments (*136–138*). The interface structures were not always perfect and could contain disconnections and other defects (Figure 7a and b). The interface equilibration process could also create threading dislocations extending into the Al grain (Figure 7c). Note that such defects can act as additional short-circuit diffusion pathways in both simulations and experiments. The unstable interfaces changed their initial orientation relationship

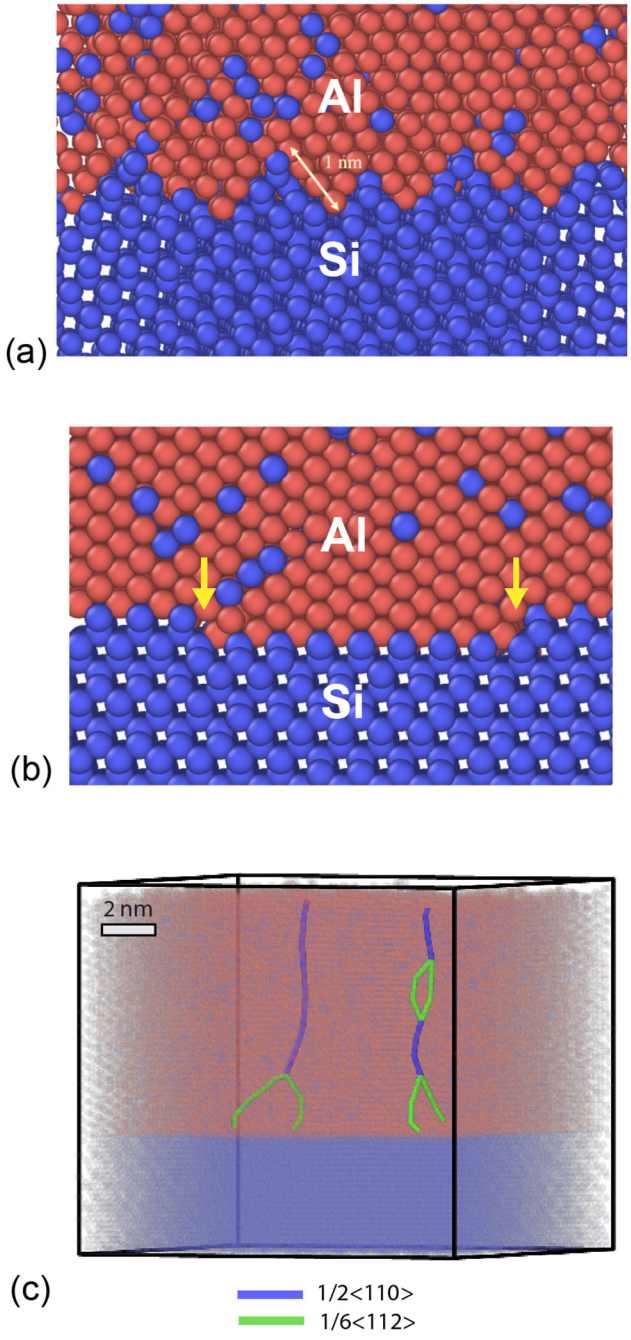

Figure 7: Examples of stable Al–Si interfaces (*90*): (a) nano-faceted $\{100\}_{Al}\|\{100\}_{Si}$ interface with cube-on-cube orientation relationship, (b) $\{110\}_{Al}\|\{100\}_{Si}$ interface with twin orientation relationship containing a disconnection dipole. The disconnections are marked by yellow arrows, (c) $\{110\}_{Al}\|\{100\}_{Si}$ interface with screw dislocations in the Al grain, which dissociate into partials at the interface.

at high temperatures. In a typical scenario, the interface would split into an IPB with a new orientation of the Al phase and a new GB in the Al phase. The new IPB was either planar or nano-faceted and remained stable at high temperatures. This process was called interface-induced recrystallization (*90*) and is illustrated in Figure 8.

4.3 Interphase diffusion coefficients and mechanisms

Diffusion in stable Al–Si interfaces was found to be very slow. During long isothermal anneals, some of the interface atoms were seen to diffuse and their diffusion mechanisms could be analyzed. However, the net atomic displacements were too small for a reliable calculation of the diffusion coefficient. The resolution of the method with respect to the diffusion coefficients is about $D = 10^{-13}$ m^2 s^{-1}. This number can be considered an upper estimate of the diffusivity in Al–Si interfaces.

Nano-faceted interfaces did not exhibit sufficient atomic mobility either. However, the $\{110\}_{Al}\|\{001\}_{Si}$ interface containing a disconnection dipole exhibited atomic mobility high enough to calculate the diffusion coefficient at several temperatures. To put the results for the Al–Si interfaces in perspective with other diffusion data in this system, they are shown on the Arrhenius diagram in Figure 9 together with the diffusivities of Al and Si in GBs and in the bulk liquid phase. The diagram also includes the lattice diffusivities and experimental data for Si diffusion in Al dislocations (*139*).

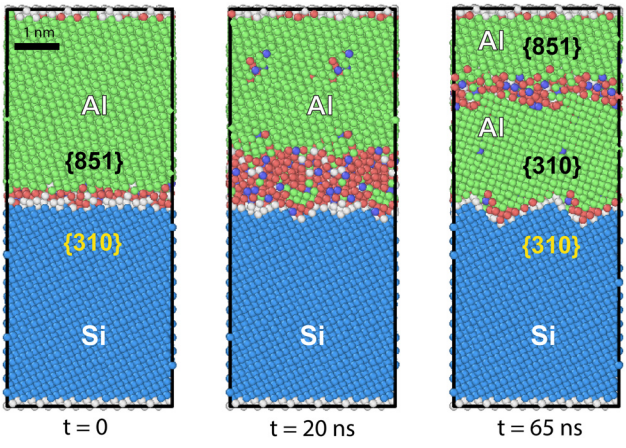

Figure 8: Interface-induced recrystallization in the Al–Si system (*90*). The numbers under the images indicate the MD simulation time: (a) initial Al–Si interface at early stages of equilibration, (b) new Al grain nucleates at the interface, (c) Si-enriched GB migrates upward into Al, leaving a faceted Al–Si interface behind. The interface orientation relationships before and after recrystallization are indicated.

The main conclusion from Figure 9 is that diffusion in Al–Si interfaces is generally slower than GB diffusion in Al. The diffusivity of atomically flat Al–Si IPBs lies below the diffusivity of even the slowest-diffusion GBs in Al (such as the Σ3 (211) incoherent twin boundary). Disconnections in the metastable interface structure accelerate diffusion of both Al and Si. But even then, the IPB diffusivity only reaches the lower end of the diffusivities in Al GBs represented by the incoherent twin and the (100)‖(110) incommensurate (IC) boundaries. The diffusivities in general high-angle GBs (such as Σ17, Σ21, and Σ45) are still significantly higher.

Diffusion mechanisms in the IPBs were found to be similar to those in GBs and were dominated by collective atomic rearrangements (*90*). Diffusion along the disconnection lines was studied in the greatest detail. It exhibited a significant dynamic heterogeneity with the formation of mobile clusters with string-like atomic displacements. Some of the strings comprised over 40 atoms. The mobile clusters had a fractal dimension of about 1.5, similar to that in GB diffusion, and were elongated along ⟨110⟩ directions. While Al atoms were the dominant participants in the strings, Si atoms also participated in collective rearrangements. Evidence suggested that Si atoms tended to interrupt the collective mechanisms preventing them from reaching larger length scales. In some cases, the MSD-time curves displayed wiggles indicative of diffusion intermittency previously observed in GB diffusion (*109*). Although the diffusion mechanisms in IPBs appeared similar to the mechanisms of GB diffusion, they were not investigated on the same level of detail, leaving much room for more detailed studies in the future.

5 Dislocation pipe diffusion

5.1 Motivation

Despite its technological importance, the phenomenon of dislocation pipe diffusion is poorly understood on the fundamental level. Accurate experimental measurements of dislocation diffusion coefficients are extremely challenging (*2, 18*). Most of the direct measurements were made in the 1960–1970s and only a few were reported in more recent times (*140–142*). There have also been indirect measurements in which the dislocation diffusivity was back-calculated from the rate of a diffusion-controlled process assumed to be controlled by dislocation diffusion. The kinetic model describing this process usually relies on crude approximations and contains other unknown parameters. Due to these uncertainties, the indirect measurements are only accurate at best up to an order of magnitude.

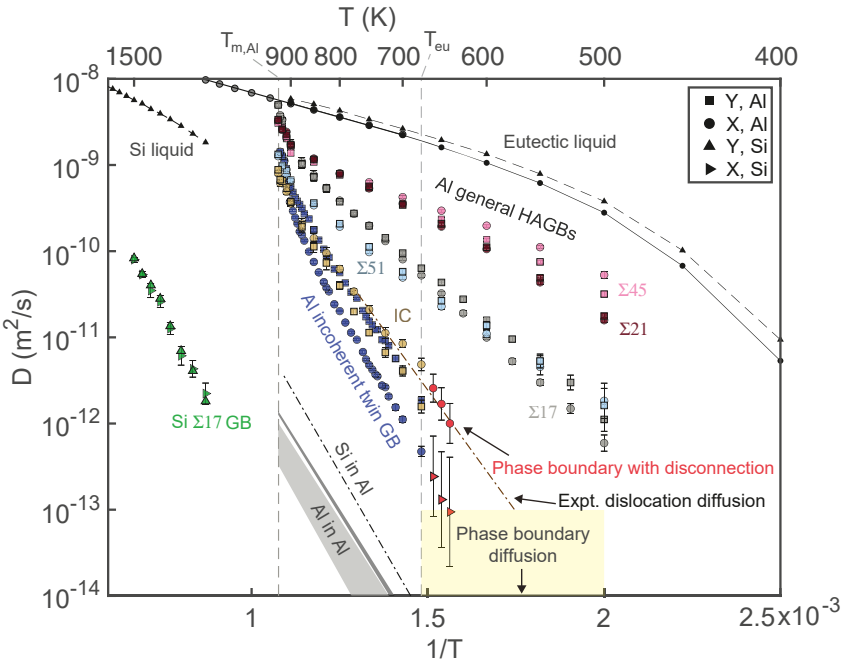

Figure 9: Arrhenius diagram of Al and Si diffusion in the Al–Si system (*90*). The yellow box indicates the upper bound of diffusivity in stable Al–Si interphase boundaries without extrinsic defects. The red symbols represent diffusion in the Al–Si interface containing a disconnection dipole. For comparison, the diagram shows simulation data for Al diffusion in Al GBs, Si diffusion in a Si GB, diffusion in liquid Si and Al–Si melt, and experimental data for lattice diffusion of Si in Al (dash-dotted line) and Al self-diffusion. Also shown is the experimental data for Si diffusion along Al dislocations (dash-dotted line) (*139*). The dashed vertical lines indicate the melting temperature of Al and the Al–Si eutectic temperature.

As with the interfaces discussed in the preceding Sections, direct MD simulations offer the most effective means of predicting the dislocation diffusion coefficients and discovering the diffusion mechanisms without *a priori* assumptions. This approach was applied to study dislocation diffusion in fcc metals such as Al (*33, 143, 144*), Ni, Cu, and Ag (*143, 144*). We will focus the discussion on the most recent atomistic study (*145*) that extended the previous work to alloy systems and examined the underlying diffusion mechanisms in more detail.

Screw and edge dislocations were studied in pure Al and Al–Si alloys with the Si concentrations of 2, 4, 6 and 8 at.% (*145*). The simulation temperatures were chosen to keep the system within the single-phase domain on the phase diagram both below and above the eutectic temperature. The dislocation was created in a cylindrical simulation block as discussed in Section 2.3 and equilibrated by hybrid MC/MD simulations. As above, the semi-empirical interatomic potential (*52*) was chosen to represent the Al–Si interactions. The dislocation diffusion coefficients were calculated from MD trajectories as discussed in Section 2.4.1. To gain insights into the diffusion mechanisms, the same statistical methods were applied as for the grain and interphase boundaries (Section 2.4.2). Further details of the simulation methodology will be reported in a forthcoming paper (*145*).

5.2 Dislocation diffusion coefficients

Both the screw and edge dislocations exhibited dynamic dissociation into Shockley partials with dissociated and undissociated (full dislocation) segments alternating along the dislocation line and in time (Figure 10). The screw dislocation had on average shorter dissociated segments with a narrower dissociation width. Alloying with Si reduced the dissociation width of both dislocations. Si was found to segregate to both dislocations forming a Cottrell atmosphere and enriching the dislocation core. The amount of segregation decreased with temperature and increased with the bulk Si concentration.

The dislocation diffusion coefficients are summarized on the Arrhenius diagrams in Figure 11a for the screw dislocation and 11b for the edge dislocation. The diffusivities of selected GBs, IPBs, and the solid and liquid bulk systems are included for comparison. The dislocation diffusivities in the alloys are only shown for representative chemical compositions to avoid overlapping the plots. The results can be summarized as follows:

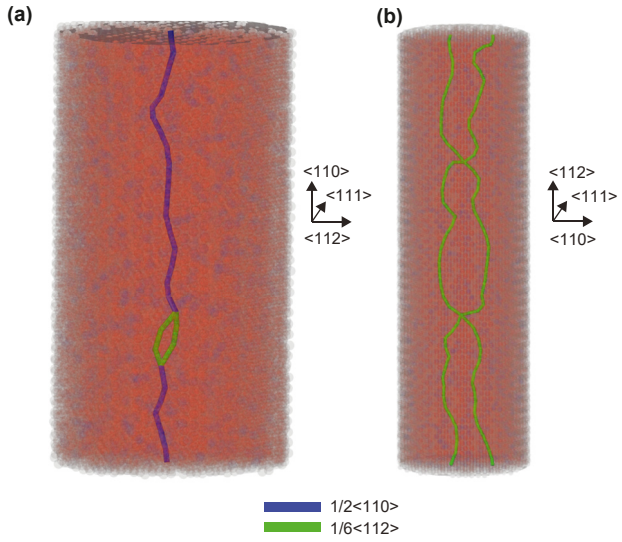

Figure 10: Representative dislocation structures in the Al–6 % Si alloy at the temperature of 700 K (*145*): (a) screw dislocation and (b) edge dislocation. The full and partial dislocation segments are shown is blue and green, respectively. The crystallographic directions in the simulation models are indicated.

- Si diffuses along the dislocations faster than Al. Note that the same trend was found for diffusion in GBs (*90*) and in the liquid phase.
- Both Al and Si dislocation diffusivities increase with bulk Si concentration. In other words, Si is a diffusion accelerator in the Al–Si system.
- In pure Al, the dislocation width δ (cf. Equation (1)) is about 0.5 nm and does not depend on the temperature within the statistical scatter of the calculations. The dislocation core does not show any signs of premelting at high temperatures. In the alloys, the Si diffusion width is larger than the Al diffusion width, $\delta_{Si} > \delta_{Al}$, especially for the edge dislocation. For the screw dislocation, δ_{Si} and δ_{Al} display no significant temperature dependence. For the edge dislocation, δ_{Si} increases with decreasing temperature and increasing Si bulk concentration and reaches approximately 1 nm in the Al–8 at.% Si alloy at low temperatures.
- The dislocation diffusion rate in pure Al is close to the lower end of the GB diffusivities. It is only at temperatures approaching the Al melting point that GB diffusion becomes faster than dislocation diffusion due to the GB premelting effect.
- Si segregation raises the dislocation diffusivity to the level of diffusion in general high-angle GBs.

The last two bullets challenge the common assumption (*2, 18*) that dislocation diffusion is slower than GB diffusion.

It is interesting to note that the Si diffusivities along the screw dislocation in the Al–(2–8) at.% Si alloy and the edge dislocation in the Al–4 at.% Si alloy are aligned with the experimental data by Legros et al. (*139*). In the experiments, the dislocation character was not resolved and the diffusivity was measured indirectly from the coarsening rates of Si precipitates in an Al matrix. Pairs of Si precipitates were studied that were connected by threading dislocations. Despite the indirect character of the measurements, the observed reasonable agreement between the simulations and the experiments is encouraging. Note also that the experimental data (*139*) is consistent with the computed Si diffusivity along the IPB containing disconnections (Section 4.3), suggesting some similarity between the diffusion processes in lattice dislocations and interface disconnections.

5.3 Dislocation diffusion mechanisms

The dislocation diffusion mechanisms were found to be similar to those in grain and interphase boundaries. At medium and high temperatures, the atomic displacements are collective and heterogeneous in space and time. The mobile atoms form clusters on the ∼10 nm length scale with a ∼1 ns lifetime. Such clusters are created by point-defect avalanches triggered by a Frenkel pair. The unit diffusive event is a collective atomic rearrangement in the form of a string and a ring.

Si atoms were observed to frequently participate in the collective mechanisms. The Si effect on the mechanisms was seen most clearly in the screw dislocation. The Si atoms often disrupted the collective events and reduced the length scale of the mobile clusters compared with pure Al. In particular, the mean string length significantly decreased with the bulk Si concentration. Si segregation also increased the fractal dimension of the mobile clusters from about 1 in pure Al to about 1.2 in the Al–8 at.% Si alloy. Diffusion in the edge dislocation exhibited a larger fractal dimension of the mobile clusters.

Diffusion intermittency was clearly observed in the screw dislocation with a periodic length of 10 nm along the dislocation line. The intermittency mostly disappeared in a longer dislocation (30 nm), suggesting that the avalanche size lies between 10 and 30 nm. During the avalanche periods, the atomic displacement field percolated all the way along the dislocation in the form of long strings. During the locked periods, little diffusion occurred except for occasional local, ring-like atomic displacements that did not percolate along the dislocation line. Intermittent behavior was not observed in the 10-nm long edge dislocation, suggesting that its dynamic length scale is smaller than 10 nm.

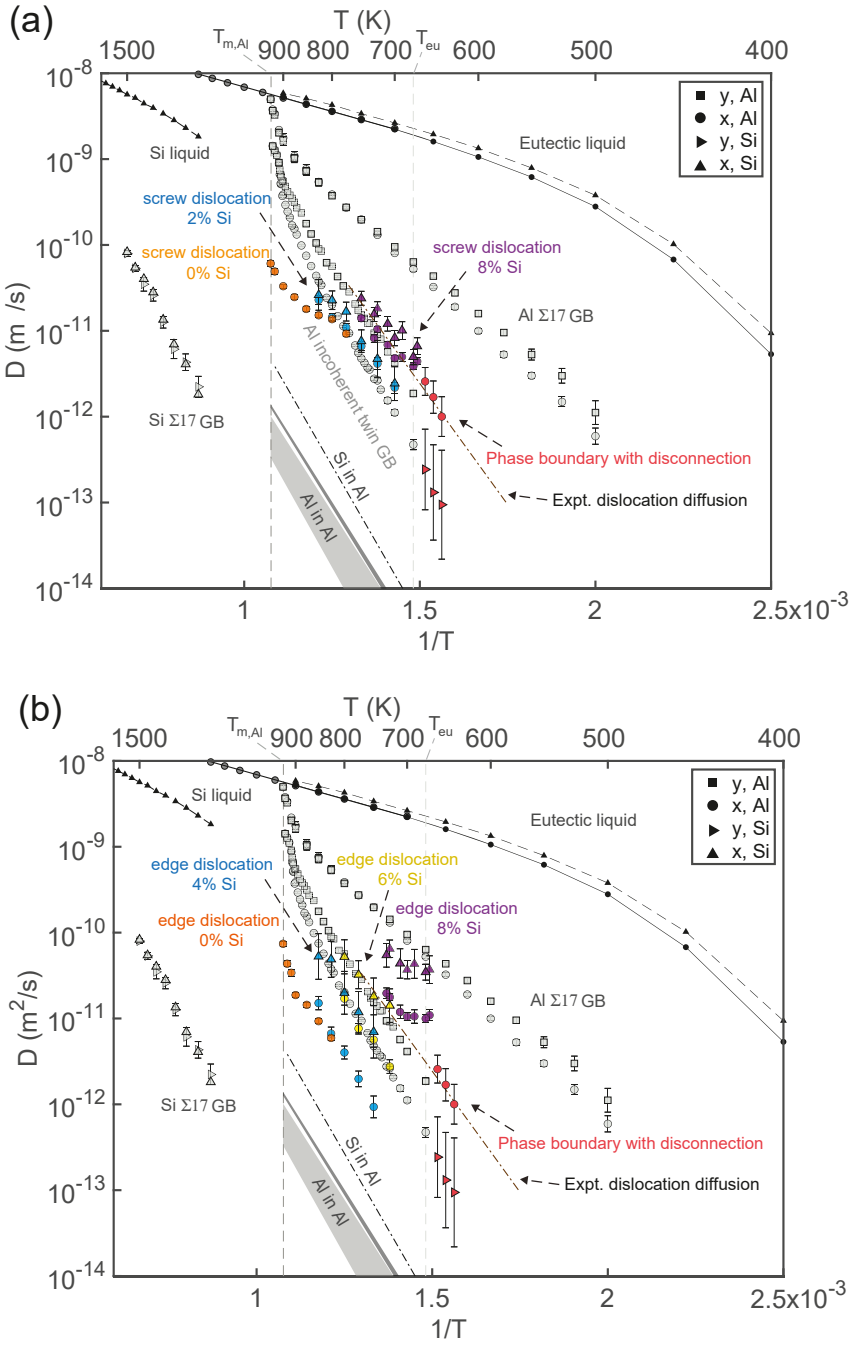

Figure 11: Arrhenius diagram of dislocation diffusion in Al and Al–Si alloys with the chemical compositions of 2, 4, and 8 at.% Si (*145*): (a) screw dislocation and (b) edge dislocation. For comparison, the diagram reproduces some of the reference data from Figure 9.

6 Conclusions and perspective

Due to the recent atomistic simulations, significant progress has been made in understanding the short-circuit diffusion in defect cores, especially the underlying atomic-level mechanisms. A major and perhaps unexpected finding is that the diffusion mechanisms in the core regions of GBs, IPBs, and dislocations are remarkably similar. At intermediate and high homologous temperatures when the core structure is partially or fully disordered, the unit diffusive events are collective atomic rearrangements. Each event involves a group of atoms moving in a strongly correlated manner. The collective atomic displacements typically occur in the form

of strings or rings. Like in bulk disordered systems, such as supercooled liquids, diffusion in defect cores exhibits dynamic heterogeneity. When measured over a short time period, the atomic displacements are distributed in space in a highly non-uniform manner. They cluster together to form a large group of mobile atoms undergoing a diffusive transition. A mobile cluster is characterized by an increased point-defect population and drastically enhanced atomic mobility. The mobile clusters have typical dimensions of about 10 nm in space and a few nanoseconds in time, although the exact numbers are system-dependent. The spontaneous formation of a mobile cluster is triggered by a local event that quickly spreads like an avalanche by a dynamic facilitation mechanism. The avalanche lifetime is presumably controlled by a kinetic transition from point-defect multiplication to point-defect annihilation. A challenge for future research is to translate this vague notion into a mathematical model describing the kinetic competition between the point-defect generation and recombination until the process reaches the bifurcation point.

The dynamic heterogeneity gives rise to intermittent diffusion behavior in nano-scale defects. Presently, this behavior is best studied in GBs (*109*) but is likely common to other defects, such as IPBs and dislocations. If the interface cross-Section or, as the case may be, the dislocation length, is comparable to the mobile cluster size, then the defect switches spontaneously between the mobile (avalanche) and immobile (locked) states in a discrete, on-and-off manner. The avalanche periods manifest themselves in surges of diffusivity and the staircase shape of the MSD-time curve. As discussed above, the diffusion intermittency can have significant implications for computer modeling of short-circuit diffusion and mass transport in nano-scale materials and devices. The effect disappears when the defect area (length) is much larger than the mobile cluster size.

The short-circuit diffusion mechanisms in alloys remain nearly unexplored. Some initial observations were mentioned above, but they barely scratch the surface. Interface/dislocation segregation of strategically chosen solutes could impact the diffusion mechanisms and enable control over the defect dynamics. Furthermore, while the previous work was focused on self-diffusion (entropy-driven diffusion in thermodynamic equilibrium), the alloy case calls for a broader study, including chemical diffusion, interdiffusion, and stress-driven co-diffusion of the alloy components. These diffusion processes can be dominated by different atomic mechanisms from self-diffusion. Uncovering such mechanisms is a promising direction for future research.

Another promising direction is further investigating diffusion along metal–nonmetal interfaces by the atomistic simulation methods applied to GBs. The recent paper (*90*) was the first step in this direction and produced interesting initial results for the Al–Si system. One of them is the realization that creating a suitable interphase boundary is a more demanding task than constructing a GB. This is an important step of the simulation procedure that can strongly impact the results of diffusion calculations. It was found that the diffusion mobilities of Al and Si atoms in stable Al–Si IPBs are much lower than in Al GBs (*90*). In fact, the IPB diffusivity in this system is so slow that it could only be calculated in the presence of interface disconnections that accelerated the interface diffusion. The diffusivity of atomically flat interfaces was beyond the capabilities of the present simulation methodology. While this null result is still helpful by providing an upper estimate of the interface diffusivity, efforts must be made to improve the capability of computer simulations to quantify small diffusion coefficients in defect cores. These results also call for a more systematic study of the impact of extrinsic defects (such as interface dislocations and disconnections) on the interface diffusivity.

It was suggested (*90*) that the slow IPB diffusion, compared to GBs, is not specific to the Al–Si system but represents a common trend for all interfaces between highly dissimilar materials with significantly different chemical bond strengths. At high homologous temperatures of Al, the homologous temperature of Si is so low that the Si atoms are virtually immobile. As a result, the Si substrate imposes a periodic potential on the interface atoms that suppresses the interface diffusivity. In contrast, the atoms diffusing along Al GBs are free from this ordering constraint and thus have a higher mobility than in the IPBs. This reasoning requires validation by studying other alloy systems and developing a more rigorous quantitative formulation in the future.

It should finally be mentioned that interface diffusion mechanisms can be impacted by interfacial phase transformations. Such transformations have been shown to cause significant changes in the GB diffusion coefficients (*146*), but their impact on the underlying diffusion mechanisms remains unexplored.

Research ethics: Not applicable.
Author contributions: All the authors have accepted responsibility for the entire content of this submitted manuscript and approved submission.
Competing interests: The authors declare no conflicts of interest regarding this article.
Research funding: This research was supported by the U.S. Department of Energy, Office of Basic Energy Sciences,

Division of Materials Sciences and Engineering, under Award # DE-SC0023102.
Data availability: Not specified.

References

1. Kaur I., Gust W., Kozma L. *Handbook of Grain and Interphase Boundary Diffusion Data*; Ziegler: Stuttgart, 1989.
2. Kaur I., Mishin Y., Gust W. *Fundamentals of Grain and Interphase Boundary Diffusion*; Wiley: Chichester, West Sussex, 1995.
3. Mishin Y., Herzig C., Bernardini J., Gust W. Grain Boundary Diffusion: Fundamentals to Recent Developments. *Int. Mater. Rev.* **1997**, *42*, 155. https://doi.org/10.1179/imr.1997.42.4.155.
4. Mishin Y., Herzig C. Grain Boundary Diffusion: Recent Progress and Future Research. *Mater. Sci. Eng. A* **1999**, *260*, 55—71. https://doi.org/10.1016/S0921-5093(98)00978-2.
5. Mishin Y., Gust W. Grain Boundary Diffusion: metals versus Non-stoichiometric Compounds. *Ionics* **2001**, *7*, 247—263. https://doi.org/10.1007/BF02373558.
6. Herzig C., Divinski S. V. Grain Boundary Diffusion in Metals: recent Developments. *Mater. Trans.* **2003**, *44*, 14—27. https://doi.org/10.2320/matertrans.44.14.
7. Herzig C., Mishin Y. Grain Boundary Diffusion in Metals. In *Diffusion in condensed matter*; Heitjans P. H. P., Kärger J., Eds. Springer Verlag: Berlin and Heidelberg, 2005; pp. 339—368.
8. Sutton A. P., Balluffi R. W. *Interfaces in Crystalline Materials*; Clarendon Press: Oxford, 1995.
9. Zhu Y., Ameyama K., Anderson P. M., Beyerlein I. J., Gao H., Kim H. S., Lavernia E., Mathaudhu S., Mughrabi H., Ritchie R. O., Tsuji N., Zhang X., Wu X. Heterostructured Materials: Superior Properties from Hetero-Zone Interaction. *Mater. Res. Lett.* **2021**, *9*, 1—31. https://doi.org/10.1080/21663831.2020.1796836.
10. Xu B., Xu W., Guo F. Creep Behavior Due to Interface Diffusion in Unidirectional Fiber-Reinforced Metal Matrix Composites under General Loading Conditions: a Micromechanics Analysis. *Acta Mech.* **2020**, *231*, 1321—1335. https://doi.org/10.1007/s00707-019-02592-8.
11. Monzen R., Asaoka J., Kita K., Kitagawa K. Influence of Alloying Elements (Ni, Co, Ag, Bi, P) on Annihilation of Orowan Loops Around Alpha-Fe Particles in Cu Matrix. *J. Jap. Inst. Metals* **1998**, *62*, 363—368. https://doi.org/10.2320/jinstmet1952.62.4-363.
12. Lesuer D. R., Syn C. K., Whittenberger J. D., Carsi M., Ruano O. A., Sherby O. D. Creep Behavior of Fe-C Alloys at High Temperatures and High Strain Rates. *Mater. Sci. Eng. A* **2001**, *317*, 101—107. https://doi.org/10.1016/S0921-5093(01)01167-4.
13. Satyanarayana D. V. V., Malakodaiah G., Sarma D. S. Stready State Creep Behavior of NiAl Hardened Austenitic Steel. *Mater. Sci. Eng. A* **2002**, *323*, 119—128. https://10.1016/S0921-5093(01)01342-9.
14. Picu R. C., Zhang D. Atomistic Study of Pipe Diffusion in Al—Mg Alloys. *Acta Mater.* **2004**, *52*, 161—171. https://doi.org/10.1016/j.actamat.2003.09.002.
15. Xu Z., Picu R. C. Dislocation-solute Cluster Interaction in Al—Mg Binary Alloys. *Model. Simul. Mater. Sci. Eng.* **2006**, *14*, 195—206. https://doi.org/10.1016/j.actamat.2003.09.002.
16. Curtin W. A., Olmsted D. L., Hector L. G. A Predictive Mechanism for Dynamic Strain Ageing of Aluminum-Magnesium Alloys. *Nat. Mater.* **2006**, *5*, 875—880. https://doi.org/10.1038/nmat1765.
17. Kolbe M., Dlouhy A., Eggeler G. Dislocation Reactions at Gamma/gamma' Interfaces during Shear Creep Deformation in the Macroscopic Crystallographic Shear System (001)[110] of CMSX6 Superalloy Single Crystals at 1025 Degrees C. *Mater. Sci. Eng. A* **1998**, *246*, 133—142. https://doi.org/10.1016/S0921-5093(97)00733-8.
18. Mehrer H. *Diffusion in Solids: Fundamentals, Methods, Materials*; Springer Verlag: Berlin, 2007.
19. Vogl G., Sepiol B. The Elementary Diffusion Step in Metals Studied by the Interference of Gamma-Rays, X-Rays and Neutrons. In *Diffusion in Condensed Matter*; Heitjans P. H. P., Kärger J., Eds. Springer Verlag: Berlin and Heidelberg, 2005; pp. 65—92.
20. Springer T., Lechner R. E. Diffusion Studies of Solids by Quasielastic Neutron Scattering. In *Diffusion in Condensed Matter*; Heitjans P. H. P., Kärger J., Eds. Springer Verlag: Berlin and Heidelberg, 2005; pp. 93—164.
21. Collins G. S., Jiang X., Bevington J. P., Selim F., Zacate M. O. Change of Diffusion Mechanism with Lattice Parameter in the Series of Lanthanide Indides Having $L1_2$ Structure. *Phys. Rev. Lett.* **2009**, *102*, 155901. https://doi.org/10.1103/PhysRevLett.102.155901.
22. Fiebig J., Divinski S., Rösner H., Estrin Y., Wilde G. Diffusion of Ag and Co in Ultrafine-Grained α-Ti Deformed by Equal Channel Angular Pressing. *J. Appl. Phys.* **2011**, *110*, 083514. https://doi.org/10.1063/1.3650230.
23. Sørensen M. R., Mishin Y., Voter A. F. Diffusion Mechanisms in Cu Grain Boundaries. *Phys. Rev. B* **2000**, *62*, 3658—3673. https://doi.org/10.1063/1.3650230.
24. A. Suzuki, Y. Mishin, Atomistic Modeling of Grain Boundary Diffusion in Fcc Metals, In *Designing of Interfacial Structures in Advanced Materials and their Joints, Hight Temperature Society of Japan*; Naka M., Ed. 2002; p. 411.
25. Suzuki A., Mishin Y. Atomistic Modeling of Point Defects and Diffusion in Copper Grain Boundaries. *Interface Sci.* **2003**, *11*, 131—148. https://doi.org/10.1023/A:1021599310093.
26. Suzuki A., Mishin Y. Interaction of Point Defects with Grain Boundaries in Fcc Metals. *Interface Sci.* **2003**, *11*, 425—437. https://doi.org/10.1023/A:1026195911339.
27. Suzuki A., Mishin Y. Diffusion Mechanisms in Grain Boundaries. *J. Metastable Nanocryst. Mater.* **2004**, *19*, 1—24. https://doi.org/10.4028/www.scientific.net/JMNM.19.1.
28. Suzuki A., Mishin Y. Atomic Mechanisms of Grain Boundary Diffusion: low versus High Temperatures. *J. Mater. Sci.* **2005**, *40*, 3155—3161. https://doi.org/10.1007/s10853-005-2678-0.
29. Boehm J., Nieminen R. M. Nose-Hoover Molecular-Dynamics Study of Self-Pipe-Diffusion in Gold Using Many-Atom Interactions. *Phys. Rev. B* **1994**, *50*, 6450—6452. [30]—[74]. https://doi.org/10.1103/PhysRevB.50.6450.
30. Hoagland R. G., Voter A. F., Foiles S. M. Self-diffusion within the Core of a Dissociated Glide Dislocation in an FCC Solid. *Scripta Mater.* **1998**, *39*, 589—596. https://doi.org/10.1016/s1359-6462(98)00201-2.
31. Fang Q. F., Wang R. Atomistic Simulation of the Atomic Structure and Diffusion within the Core Region of an Edge Dislocation in Aluminum. *Phys. Rev. B* **2000**, *62*, 9317—9324. https://doi.org/10.1103/physrevb.62.9317.
32. Jannot E., Mohles V., Gottstein G., Thijsse B. Atomistic Simulation of Pipe Diffusion in AlCu Alloys. *Defect Diffusion Forum* **2006**, *249*, 47—54. https://doi.org/10.4028/www.scientific.net/ddf.249.47.

33. Pun G. P. P., Mishin Y. A Molecular Dynamics Study of Self-Diffusion in the Cores of Screw and Edge Dislocations in Aluminum. *Acta Mater.* **2009**, *57*, 5531—5542. https://doi.org/10.1016/j.actamat.2009.07.048.
34. Brenner D. W. The Art and Science of an Analytical Potential. *Phys. Status Solidi* **2000**, *217*, 23—40. https://doi.org/10.1002/(sici)1521-3951(200001)217:1&tnqx3c;23::aid-pssb23&tnqx3e;3.0.co;2-n.
35. Mishin Y. Interatomic Potentials for Metals. In *Handbook of Materials Modeling*; Yip S., Ed. Springer: Dordrecht, The Netherlands, 2005; pp. 459—478.
36. Mishin Y., Asta M., Li J. Atomistic Modeling of Interfaces and Their Impact on Microstructure and Properties. *Acta Mater.* **2010**, *58*, 1117—1151. https://doi.org/10.1016/j.actamat.2009.10.049.
37. Mishin Y. Machine-Learning Interatomic Potentials for Materials Science. *Acta Mater.* **2021**, *214*, 116980. https://doi.org/10.2139/ssrn.3787885.
38. Daw M. S., Baskes M. I. Semiempirical, Quantum Mechanical Calculation of Hydrogen Embrittlement in Metals. *Phys. Rev. Lett.* **1983**, *50*, 1285—1288. https://doi.org/10.1103/physrevlett.50.1285.
39. Daw M. S., Baskes M. I. Embedded-Atom Method: Derivation and Application to Impurities, Surfaces, and Other Defects in Metals. *Phys. Rev. B* **1984**, *29*, 6443—6453. https://doi.org/10.1103/physrevb.29.6443.
40. Finnis M. W., Sinclair J. E. A Simple Empirical N-Body Potential for Transition Metals. *Philos. Mag. A* **1984**, *50*, 45—55. https://doi.org/10.1080/01418618408244210.
41. Baskes M. I. Application of the Embedded-Atom Method to Covalent Materials: a Semi-empirical Potential for Silicon. *Phys. Rev. Lett.* **1987**, *59*, 2666—2669. https://doi.org/10.1103/physrevlett.59.2666.
42. Mishin Y., Mehl M. J., Papaconstantopoulos D. A. Phase Stability in the Fe-Ni System: investigation by First-Principles Calculations and Atomistic Simulations. *Acta Mater.* **2005**, *53*, 4029—4041. https://doi.org/10.1016/j.actamat.2005.05.001.
43. Lysogorskiy Y., Hammerschmidt T., Janssen J., Neugebauer J., Drautz R. Transferability of Interatomic Potentials for Molybdenum and Silicon. *Model. Simul. Mater. Sci. Eng.* **2019**, *27*, 025007. https://doi.org/10.1088/1361-651x/aafd13.
44. Drautz R. Atomic Cluster Expansion for Accurate and Transferable Interatomic Potentials. *Phys. Rev. B* **2019**, *99*, 014104. https://doi.org/10.1103/physrevb.99.014104.
45. Drautz R. Atomic Cluster Expansion of Scalar, Vectorial, and Tensorial Properties Including Magnetism and Charge Transfer. *Phys. Rev. B* **2020**, *102*, 024104. https://doi.org/10.1103/physrevb.102.024104.
46. Tersoff J. New Empirical Approach for the Structure and Energy of Covalent Systems. *Phys. Rev. B* **1988**, *37*, 6991—7000. https://doi.org/10.1103/physrevb.37.6991.
47. Tersoff J. Empirical Interatomic Potential for Silicon with Improved Elastic Properties. *Phys. Rev. B* **1988**, *38*, 9902—9905. https://doi.org/10.1103/physrevb.38.9902.
48. Tersoff J. Modeling Solid-State Chemistry: interatomic Potentials for Multicomponent Systems. *Phys. Rev. B* **1989**, *39*, 5566—5568. https://doi.org/10.1103/physrevb.39.5566.
49. Stillinger F. H., Weber T. A. Computer Simulation of Local Order in Condensed Phases of Silicon. *Phys. Rev. B* **1985**, *31*, 5262—5271. https://doi.org/10.1103/physrevb.31.5262.
50. Dongare A. M., Neurock M., Zhigilei L. V. Angular-dependent Embedded Atom Method Potential for Atomistic Simulations of Metal-Covalent Systems. *Phys. Rev. B* **2009**, *80*, 184106. https://doi.org/10.1103/physrevb.80.184106.
51. Dongare A. M., Zhigilei L. V., Rajendran A. M., LaMattina B. Interatomic Potentials for Atomic Scale Modeling of Metal—Matrix Ceramic Particle Reinforced Nanocomposites. *Composites, Part B* **2009**, *40*, 461—467. https://doi.org/10.1016/j.compositesb.2009.02.001.
52. Saidi P., Frolov T., Hoyt J. J., Asta M. An Angular Embedded Atom Method Interatomic Potential for the Aluminum—Silicon System. *Model. Simul. Mater. Sci. Eng.* **2014**, *22*, 055010. https://doi.org/10.1088/0965-0393/22/5/055010.
53. M. Payne, G. Csanyi, A. de Vita, Hybrid Atomistic Modelling of Materials Processes, In *Handbook of Materials Modeling*; Yip S., Ed. Springer: Dordrecht, The Netherlands, 2005; pp. 2763—2770.
54. Bartok A., Payne M. C., Kondor R., Csanyi G. Gaussian Approximation Potentials: the Accuracy of Quantum Mechanics, without the Electrons. *Phys. Rev. Lett.* **2010**, *104*, 136403. https://doi.org/10.1103/physrevlett.104.136403.
55. Bartok A. P., Kondor R., Csanyi G. On Representing Chemical Environments. *Phys. Rev. B* **2013**, *87*, 219902. https://doi.org/10.1103/physrevb.87.184115.
56. Li Z., Kermode J. R., De Vita A. Molecular Dynamics with On-The-Fly Machine Learning of Quantum-Mechanical Forces. *Phys. Rev. Lett.* **2015**, *114*, 096405. https://doi.org/10.1103/physrevlett.114.096405.
57. Glielmo A., Sollich P., De Vita A. Accurate Interatomic Force Fields via Machine Learning with Covariant Kernels. *Phys. Rev. B* **2017**, *95*, 214302. https://doi.org/10.1103/physrevb.95.214302.
58. Bartok A. P., Kermore J., Bernstein N., Csanyi G. Machine Learning a General Purpose Interatomic Potential for Silicon. *Phys. Rev. X* **2018**, *8*, 041048. https://doi.org/10.1103/physrevx.8.041048.
59. Deringer V. L., Pickard C. J., Csanyi G. Data-driven Learning of Total and Local Energies in Elemental Boron. *Phys. Rev. Lett.* **2018**, *120*, 156001. https://doi.org/10.1103/physrevlett.120.156001.
60. Botu V., Ramprasad R. Adaptive Machine Learning Framework to Accelerate Ab Initio Molecular Dynamics. *Int. J. Quant. Chem.* **2015**, *115*, 1074—1083. https://doi.org/10.1002/qua.24836.
61. Botu V., Ramprasad R. Learning Scheme to Predict Atomic Forces and Accelerate Materials Simulations. *Phys. Rev. B* **2015**, *92*, 094306. https://doi.org/10.1103/physrevb.92.094306.
62. Mueller T., Kusne A. G., Ramprasad R. Machine Learning in Materials Science: recent Progress and Emerging Applications. In *Reviews in Computational Chemistry*; Parrill A. L., Lipkowitz K. B., Eds.; Wiley, Vol. 29, 2016; pp. 186—273.
63. Behler J., Parrinello M. Generalized Neural-Network Representation of High-Dimensional Potential-Energy Surfaces. *Phys. Rev. Lett.* **2007**, *98*, 146401. https://doi.org/10.1103/physrevlett.98.146401.
64. Bholoa A., Kenny S. D., Smith R. A New Approach to Potential Fitting Using Neural Networks. *Nucl. Instrum. Methods Phys. Res.* **2007**, *255*, 1—7. https://doi.org/10.1016/nimb.2006.11.040.
65. Behler J., Martonak R., Donadio D., Parrinello M. Metadynamics Simulations of the High-Pressure Phases of Silicon Employing a High-Dimensional Neural Network Potential. *Phys. Rev. Lett.* **2008**, *100*, 185501. https://doi.org/10.1103/physrevlett.100.185501.

66. Sanville E., Bholoa A., Smith R., Kenny S. D. Silicon Potentials Investigated Using Density Functional Theory Fitted Neural Networks. *J. Phys.: Condens. Matter* **2008**, *20*, 285219. https://doi.org/10.1088/0953-8984/20/28/285219.
67. Eshet H., Khaliullin R. Z., Kuhle T. D., Behler J., Parrinello M. Ab Initio Quality Neural-Network Potential for Sodium. *Phys. Rev. B* **2010**, *81*, 184107. https://doi.org/10.1103/physrevb.81.184107.
68. Handley C. M., Popelier P. L. A. Potential Energy Surfaces Fitted by Artificial Neural Networks. *J. Phys. Chem. A* **2010**, *114*, 3371−3383. https://doi.org/10.1021/jp9105585.
69. Behler J. Neural Network Potential-Energy Surfaces in Chemistry: a Tool for Large-Scale Simulations. *Phys. Chem. Chem. Phys.* **2011**, *13*, 17930−17955. https://doi.org/10.1039/c1cp21668f.
70. Behler J. Atom-centered Symmetry Functions for Constructing High-Dimensional Neural Network Potentials. *J. Chem. Phys.* **2011**, *134*, 074106. https://doi.org/10.1063/1.3553717.
71. Sosso G. C., Miceli G., Caravati S., Behler J., Bernasconi M. Neural Network Interatomic Potential for the Phase Change Material GeTe. *Phys. Rev. B* **2012**, *85*, 174103. https://doi.org/10.1103/physrevb.85.174103.
72. Behler J. Constructing High-Dimensional Neural Network Potentials: a Tutorial Review. *Int. J. Quant. Chem.* **2015**, *115*, 1032−1050. https://doi.org/10.1002/qua.24890.
73. Behler J. Perspective: machine Learning Potentials for Atomistic Simulations. *Phys. Chem. Chem. Phys.* **2016**, *145*, 170901. https://doi.org/10.1063/1.4966192.
74. Imbalzano G., Anelli A., Giofre D., Klees S., Behler J., Ceriotti M. Automatic Selection of Atomic Fingerprints and Reference Configurations for Machine-Learning Potentials. *J. Chem. Phys.* **2018**, *148*, 241730. https://doi.org/10.1063/1.5024611.
75. Purja Pun G. P., Batra R., Ramprasad R., Mishin Y. Physically Informed Artificial Neural Networks for Atomistic Modeling of Materials. *Nat. Commun.* **2019**, *10*, 2339. https://doi.org/10.1038/s41467-019-10343-5.
76. Pun G. P. P., Yamakov V., Hickman J., Glaessgen E. H., Mishin Y. Development of a General-Purpose Machine-Learning Interatomic Potential for Aluminum by the Physically Informed Neural Network Method. *Phys. Rev. Mater.* **2020**, *4*, 113807. https://doi.org/10.1103/PhysRevMaterials.4.113807.
77. Lin Y.-S., Pun G. P. P., Mishin Y. Development of a Physically-Informed Neural Network Interatomic Potential for Tantalum. *Comput. Mater. Sci.* **2022**, *205*, 111180. https://doi.org/10.1016/j.commatsci.2021.111180.
78. Thompson A., Swiler L., Trott C., Foiles S., Tucker G. Spectral Neighbor Analysis Method for Automated Generation of Quantum-Accurate Interatomic Potentials. *J. Comput. Phys.* **2015**, *285*, 316−330. https://doi.org/10.1016/j.jcp.2014.12.018.
79. Chen C., Deng Z., Tran R., Tang H., Chu I.-H., Ong S. P. Accurate Force Field for Molybdenum by Machine Learning Large Materials Data. *Phys. Rev. Mater.* **2017**, *1*, 043603. https://doi.org/10.1103/PhysRevMaterials.1.043603.
80. Li X.-G., Hu C., Chen C., Deng Z., Luo J., Ong S. P. Quantum-accurate Spectral Neighbor Analysis Potential Models for Ni-Mo Binary Alloys and Fcc Metals. *Phys. Rev. B* **2018**, *98*, 094104. https://doi.org/10.1103/PhysRevB.98.094104.
81. Shapeev A. V. Moment Tensor Potentials: a Class of Systematically Improvable Interatomic Potentials. *Multiscale Model. Simul.* **2016**, *14*, 1153−1173. https://doi.org/10.1137/15M1054183.
82. Olmsted D. L., Holm E. A., Foiles S. M. Survey of Computed Grain Boundary Properties in Face-Centered Cubic Metals-II: grain Boundary Mobility. *Acta Mater.* **2009**, *57*, 3704−3713. https://doi.org/10.1016/j.actamat.2009.04.015.
83. Tschopp M. A., Coleman S. P., McDowell D. L. Symmetric and Asymmetric Tilt Grain Boundary Structure and Energy in Cu and Al (And Transferability to Other Fcc Metals). *Integr. Mater. Manuf. Innov.* **2015**, *4*, 11. https://doi.org/10.1080/14786430701455321.
84. Frolov T., Olmsted D. L., Asta M., Mishin Y. Structural Phase Transformations in Metallic Grain Boundaries. *Nat. Commun.* **2013**, *4*, 1899. https://doi.org/10.1038/ncomms2919.
85. Hickman J., Mishin Y. Extra Variable in Grain Boundary Description. *Phys. Rev. Mater.* **2017**, *1*, 010601. https://doi.org/10.1103/PhysRevMaterials.1.010601.
86. Yang C., Zhang M., Qi L. Grain Boundary Structure Search by Using an Evolutionary Algorithm with Effective Mutation Methods. *Comput. Mater. Sci.* **2020**, *184*, 109812. https://doi.org/10.1016/j.commatsci.2020.109812.
87. Koju R. K., Mishin Y. Relationship between Grain Boundary Segregation and Grain Boundary Diffusion in Cu-Ag Alloys. *Phys. Rev. Mater.* **2020**, *4*, 073403. https://doi.org/10.1103/PhysRevMaterials.4.073403.
88. Koju R. K., Mishin Y. Atomistic Study of Grain-Boundary Segregation and Grain-Boundary Diffusion in Al−Mg Alloys. *Acta Mater.* **2020**, *201*, 596−603. https://doi.org/10.1016/j.actamat.2020.10.029.
89. Koju R. K., Mishin Y. The Role of Grain Boundary Diffusion in the Solute Drag Effect. *Nanomaterials* **2021**, *11*, 2348. https://doi.org/10.3390/nano11092348.
90. Chesser I., Koju R., Vellore A., Mishin Y. Atomistic Modeling of Metal-Nonmetal Interphase Boundary Diffusion. *Acta Mater.* **2023**, *257*, 119172. https://doi.org/10.1016/j.actamat.2023.119172.
91. Stroh A. N. Dislocations and Cracks in Anisotropic Elasticity. *Philos. Mag.* **1958**, *3*, 625−646. https://doi.org/10.1080/14786435808565804.
92. Stroh A. N. Steady State Problems in Anisotropic Elasticity. *J. Math. Phys.* **1962**, *41*, 77−103. https://doi.org/10.1002/sapm196241177.
93. Mishin Y. Calculation of Open and Closed System Elastic Coefficients for Multicomponent Solids. *Phys. Rev. B* **2015**, *91*, 224107. https://doi.org/10.1103/PhysRevB.91.224107.
94. Mishin Y., Cahn J. W. Thermodynamics of Cottrell Atmospheres Tested by Atomistic Simulations. *Acta Mater.* **2016**, *117*, 197−206. https://doi.org/10.1016/j.actamat.2016.07.013.
95. Plimpton S. Fast Parallel Algorithms for Short-Range Molecular-Dynamics. *J. Comput. Phys.* **1995**, *117*, 1−19. https://doi.org/10.1006/jcph.1995.1039.
96. V. Yamakov, *The ParaGrandMC Code can be Obtained from the NASA Software Catalog*, 2016. https://software.nasa.gov/software/LAR-18773-1,NASA/CR&tnqx2013;2016-219202. URL: https://software.nasa.gov/software/LAR-19893-1.
97. Purja Pun G. P., Yamakov V., Mishin Y. Interatomic Potential for the Ternary Ni−Al−Co System and Application to Atomistic Modeling of the B2−$L1_0$ Martensitic Transformation. *Model. Simul. Mater. Sci. Eng.* **2015**, *23*, 065006. https://doi.org/10.1088/0965-0393/23/6/065006.
98. Yamakov V., Hochhalter J. D., Leser W. P., Warner J. E., Newman J. A., Purja Pun G. P., Mishin Y. Multiscale Modeling of Sensory Properties of Co−ni−al Shape Memory Particles Embedded in an

Al Metal Matrix. *J. Mater. Sci.* **2016**, *51*, 1204–1216. https://doi.org/10.1007/s10853-015-9153-3.
99. Stukowski A. Visualization and Analysis of Atomistic Simulation Data with OVITO – the Open Visualization Tool. *Model. Simul. Mater. Sci. Eng* **2010**, *18*, 015012. https://doi.org/10.1088/0965-0393/18/1/015012.
100. Donati C., Glotzer S. C., Poole P. H., Kob W., Plimpton S. J. Spatial Correlations of Mobility and Immobility in a Glass-Forming Lennard-Jones Liquid. *Phys. Rev. B* **1999**, *60*, 3107–3119. https://doi.org/10.1103/PhysRevE.60.3107.
101. Donati C., Douglas J. F., Kob W., Plimpton S. J., Poole P. H., Glotzer S. C. Stringlike Cooperative Motion in a Supercooled Liquid. *Phys. Rev. Lett.* **1998**, *80*, 2338–2341. https://doi.org/10.1103/PhysRevLett.80.2338.
102. Zhang H., Srolovitz D. J., Douglas J. F., Warren J. A. Characterization of Atomic Motion Governing Grain Boundary Migration. *Phys. Rev. B* **2006**, *74*, 115404. https://link.aps.org/doi/10.1103/PhysRevB.74.115404.
103. Zhang H., Srolovitz D. J., Douglas J. F., Warren J. A. Atomic Motion during the Migration of General [001] Tilt Grain Boundaries in Ni. *Acta Mater.* **2007**, *55*, 4527–4533. https://doi.org/10.1016/j.actamat.2007.04.015.
104. Zhang H., Douglas J. F., Srolovitz D. J., Warren J. A. Grain Boundaries Exhibit the Dynamics of Glass-Forming Liquids. *Proc. Natl. Acad. Sci. U. S. A.* **2009**, *106*, 7735–7740. https://doi.org/10.1073/pnas.0900227106.
105. Zhang H., Kalvapalle P., Douglas J. F. String-like Collective Atomic Motion in the Interfacial Dynamics of Nanoparticles. *Soft Matter* **2010**, *6*, 5944–5955. https://doi.org/10.1021/jp203765x.
106. Zhang H., Khalkhali M., Liu Q., Douglas J. F. String-like Cooperative Motion in Homogeneous Melting. *J. Chem. Phys.* **2013**, *138*, 12A538. https://doi.org/10.1063/1.4769267.
107. Zhang H., Wang X., Yu H.-B., Douglas J. F. Dynamic Heterogeneity, Cooperative Motion, and Johari–Goldstein β Relaxation in a Metallic Glass-Forming Material Exhibiting a Fragile-To-Strong Transition. *Eur. Phys. J. E* **2021**, *44*, 1–30. https://doi.org/10.1140/epje/s10189-021-00060-7.
108. Koju R., Mishin Y. Direct Atomistic Modeling of Solute Drag by Moving Grain Boundaries. *Acta Mater.* **2020**, *198*, 111–120. https://doi.org/10.1016/j.actamat.2020.07.052.
109. Chesser I., Mishin Y. Point-Defect Avalanches Mediate Grain Boundary Diffusion. *Commun. Mater.* **2022**, *3*, 90. https://doi.org/10.1038/s43246-022-00314-7.
110. Mishin Y. An Atomistic View of Grain Boundary Diffusion. *Defect Diffusion Forum* **2015**, *363*, 1–11. https://doi.org/10.4028/www.scientific.net/DDF.363.1.
111. Suzuki A., Mishin Y. Atomic Mechanisms of Grain Boundary Motion. *Mater. Sci. Forum* **2005**, *502*, 157–162. https://doi.org/10.4028/www.scientific.net/MSF.502.157.
112. Starikov S., Mrovec M., Drautz R. Study of Grain Boundary Self-Diffusion in Iron with Different Atomistic Models. *Acta Mater.* **2020**, *188*, 560–569. https://doi.org/10.1016/j.actamat.2020.02.027.
113. Hickman J., Mishin Y. Disjoining Potential and Grain Boundary Premelting in Binary Alloys. *Phys. Rev. B* **2016**, *93*, 224108. https://doi.org/10.1103/PhysRevB.93.224108.
114. Mishin Y., Boettinger W. J., Warren J. A., McFadden G. B. Thermodynamics of Grain Boundary Premelting in Alloys. I. Phase Field Modeling. *Acta Mater.* **2009**, *57*, 3771–3785. https://doi.org/10.1016/j.actamat.2009.04.044.
115. Williams P. L., Mishin Y. Thermodynamics of Grain Boundary Premelting in Alloys. II. Atomistic Simulation. *Acta Mater.* **2009**, *57*, 3786–3794. https://doi.org/10.1016/j.actamat.2009.04.037.
116. Annamareddy A., Eapen J. Low Dimensional String-like Relaxation Underpins Superionic Conduction in Fluorites and Related Structures. *Sci. Rep.* **2017**, *7*, 1–12. https://doi.org/10.1038/srep44149.
117. Fransson E., Erhart P. Defects from Phonons: atomic Transport by Concerted Motion in Simple Crystalline Metals. *Acta Mater.* **2020**, *196*, 770–775. https://doi.org/10.1016/j.actamat.2020.06.040.
118. Jung Y., Garrahan J. P., Chandler D. Dynamical Exchanges in Facilitated Models of Supercooled Liquids. *J. Chem. Phys.* **2005**, *123*, 084509. https://doi.org/10.1063/1.2001629.
119. Pan A. C., Garrahan J. P., Chandler D. Heterogeneity and Growing Length Scales in the Dynamics of Kinetically Constrained Lattice Gases in Two Dimensions. *Phys. Rev. E* **2005**, *72*, 041106. https://doi.org/10.1103/PhysRevE.72.041106.
120. Chandler D., Garrahan J. P. Dynamics on the Way to Forming Glass: bubbles in Space-Time. *Annu. Rev. Phys. Chem.* **2010**, *61*, 191–217. https://doi.org/10.1146/annurev.physchem.040808.090405.
121. Smirnova D., Starikov S., Leines G. D., Liang Y., Wang N., Popov M. N., Abrikosov I. A., Sangiovanni D. G., Drautz R., Mrovec M. Atomistic Description of Self-Diffusion in Molybdenum: a Comparative Theoretical Study of Non-Arrhenius Behavior. *Phys. Rev. Mater.* **2020**, *4*, 013605. https://doi.org/10.1103/PhysRevMaterials.4.013605.
122. Starikov S., Jamebozorgi V., Smirnova D., Drautz R., Mrovec M. Atomistic Simulations of Pipe Diffusion in Bcc Transition Metals. *Acta Mater.* **2023**, *260*, 119294. https://doi.org/10.1016/j.actamat.2023.119294.
123. Sommer J., Muschik T., Herzig C., Gust W. Silver Tracer Diffusion in Oriented AgCu Interphase Boundaries and Correlation to the Boundary Structure. *Acta Mater.* **1996**, *44*, 327–334. https://doi.org/10.1016/1359-6454(95)00166-2.
124. Minkwitz C., Herzig C., Straumal B. B., Gust W. Radiotracer Diffusion of Ni and Ag in Ag and Ni Grain Boundaries and Oriented Ag/Ni Interphase Boundaries. *Mater. Sci. Forum* **1998**, *294–296*, 541–544. https://doi.org/10.4028/www.scientific.net/MSF.294-296.541.
125. Straumal B. B., Klinger L. M., Shvindlerman L. S. The Effect of Crystallographic Parameters of Interphase Boundaries on Their Surface Tension and Parameters of the Boundary Diffusion. *Acta Metall.* **1984**, *32*, 1355–1364. https://doi.org/10.1016/0001-6160(84)90081-6.
126. Kosinova A., Kovalenko O., Klinger L., Rabkin E. Mechanisms of Solid-State Dewetting of Thin Au Films in Different Annealing Atmospheres. *Acta Mater.* **2015**, *83*, 91–101. https://doi.org/10.1016/j.actamat.2014.09.049.
127. Kumar A., Barda H., Klinger L., Finnis M. W., Lordi V., Rabkin E., Srolovitz D. J. Anomalous Diffusion along Metal/ceramic Interfaces. *Nat. Commun.* **2018**, *9*, 5251. https://doi.org/10.1038/s41467-018-07724-7.
128. Barda H., Rabkin E. Metal Hetero-Diffusion along the Metal-Ceramic Interfaces: a Case Study of Au Diffusion along the

Ni-Sapphire Interface. *Acta Mater.* **2020**, *186*, 242—249. https://doi.org/10.1016/j.actamat.2019.12.051.
129. Rösler J., Bao G., Evans A. G. The Effects of Diffusional Relaxation on the Creep Strength of Composites. *Acta Metall. Mater.* **1991**, *39*, 2733—2738. https://doi.org/10.1016/0956-7151(91)90090-N.
130. Mendelev M. I., Kramer M. J., Becker C. A., Asta M. Analysis of Semi-empirical Interatomic Potentials Appropriate for Simulations of Crystalline and Liquid Al and Cu. *Philos. Mag.* **2008**, *68*, 1723—1750. https://doi.org/10.1080/14786430802206482.
131. Dongare A. M., LaMattina B., Irving D. L., Rajendran A. M., Zikry M. A., Brenner D. W. An Angular-dependent Embedded Atom Method (A-EAM) Interatomic Potential to Model Thermodynamic and Mechanical Behavior of Al/Si Composite Materials. *Model. Simul. Mater. Sci. Eng.* **2012**, *20*, 035007. https://doi.org/10.1088/0965-0393/20/3/035007.
132. Mishin Y. Atomistic Modeling of the γ and γ' Phases of the Ni-Al System. *Acta Mater.* **2004**, *52*, 1451—1467. https://doi.org/10.1016/j.actamat.2003.11.026.
133. Williams P. L., Mishin Y., Hamilton J. C. An Embedded-Atom Potential for the Cu-Ag System. *Model. Simul. Mater. Sci. Eng.* **2006**, *14*, 817—833. https://doi.org/10.1088/0965-0393/14/5/002.
134. Purja Pun G. P., Mishin Y. Development of an Interatomic Potential for the Ni-Al System. *Philos. Mag.* **2009**, *89*, 3245—3267. https://doi.org/10.1080/14786430903258184.
135. Howells C. A., Mishin Y. Angular-dependent Interatomic Potential for the Binary Ni-Cr System. *Model. Simul. Mater. Sci. Eng.* **2018**, *26*, 085008. https://doi.org/10.1088/1361-651X/aae400.
136. Westmacott K., Hinderberger S., Dahmen U. Physical Vapour Deposition Growth and Transmission Electron Microscopy Characterization of Epitaxial Thin Metal Films on Single-Crystal Si and Ge Substrates. *Philos. Mag. A* **2001**, *81*, 1547—1578. https://doi.org/10.1080/01418610108214362.
137. Thangaraj N., Westmacott K., Dahmen U. Epitaxial Growth of (011) Al on (100) Si by Vapor Deposition. *Appl. Phys. Lett.* **1992**, *61*, 37—39. https://doi.org/10.1063/1.107660.
138. McSkimming B. M., Alexander A., Samuels M. H., Arey B., Arslan I., Richardson C. J. Metamorphic Growth of Relaxed Single Crystalline Aluminum on Silicon (111). *J. Vac. Sci. Technol., A* **2017**, *35*, 021401. https://doi.org/10.1116/1.4971200.
139. Legros M., Dehm G., Arzt E., Balk T. J. Observation of Giant Diffusivity along Dislocation Cores. *Science* **2008**, *319*, 1646—1649. https://doi.org/10.1126/science.1151771.
140. Ishikawa T., McLellan R. B. The Diffusivity of Hydrogen in Aluminum. *Acta Metall.* **1986**, *34*, 1091. https://doi.org/10.1016/0001-6160(86)90219-1.
141. Sakaguchi I., Yurimoto H., Sueno S. Self-Diffusion Along Dislocations in Single-Crystal MgO. *Solid State Commun.* **1992**, *84*, 889—893. https://doi.org/10.1016/0038-1098(92)90453-G.
142. Nakagawa T., Nakamura A., Sakaguchi I., Shibata N., Peter K., Lagerlöf D., Yamamoto T., Haneda H., Ikuhara Y. Oxygen Pipe Diffusion in Sapphire Basal Dislocation. *J. Ceram. Soc. Jpn* **2006**, *114*, 1013—1017. https://doi.org/10.2109/jcersj.114.1013.
143. Soltani S., Abdolrahim N., Sepehrband P. Molecular Dynamics Study of Self-Diffusion in the Core of a Screw Dislocation in Face Centered Cubic Crystals. *Scr. Mater.* **2017**, *133*, 101—104. https://doi.org/10.1016/j.scriptamat.2017.02.021.
144. Soltani S., Abdolrahim N., Sepehrband P. Mechanism of Intrinsic Diffusion in the Core of Screw Dislocations in FCC Metals—A Molecular Dynamics Study. *Comput. Mater. Sci.* **2018**, *144*, 50—55. https://doi.org/10.1016/j.commatsci.2017.11.048.
145. Chesser I., Koju R., Mishin Y. *An Atomistic Study of Dislocation Diffusion in Al-Si Alloys*, 2023, to be published.
146. Frolov T., Divinski S. V., Asta M., Mishin Y. Effect of Interface Phase Transformations on Diffusion and Segregation in High-Angle Grain Boundaries. *Phys. Rev. Lett.* **2013**, *110*, 255502. https://doi.org/10.1103/PhysRevLett.110.255502.